GEOPHYSICS, VOL. 87, NO. 4 (JULY-AUGUST 2022); P. E219–E241, 15 FIGS., 1 TABLE.
10.1190/GEO2021-0328.1

A cost-effective three-dimensional marine controlled-source electromagnetic survey: Exploring seafloor massive sulfides

Keiichi Ishizu[1], Weerachai Siripunvaraporn[2], Tada-nori Goto[3], Katsuaki Koike[4], Takafumi Kasaya[5], and Hisanori Iwamoto[6]

ABSTRACT

A 3D marine controlled-source electromagnetic (CSEM) survey for mapping hydrocarbons uses dozens of ocean-bottom electric (OBE) receivers deployed in a grid pattern and several transmitter towlines. This study considers seafloor massive sulfides (SMS) exploration, and the horizontal survey scale of SMS is a few kilometers, which is small compared with hydrocarbon surveys of tens of kilometers. If we apply a 3D CSEM survey using a receiver deployment on grids to map SMS, high survey costs will be incurred despite the small survey size. We have developed a cost-effective 3D marine CSEM survey that uses fewer receivers than the survey with a receiver deployment on grids to reduce survey costs for SMS. This CSEM survey uses a line of OBE receivers in the center of the survey area and several transmitter towlines. Numerical tests demonstrate that our survey (seven OBE receivers) using 80% fewer receivers than the survey with a receiver deployment on grids (35 OBE receivers) is able to accurately map SMS, obtaining a performance similar to that of the receiver deployment on grids. Then, we explore SMS in the Ieyama hydrothermal area off Okinawa, southwest Japan, using our 3D CSEM survey with a line of six OBE receivers and three transmitter towlines. The resulting 3D resistivity distribution from the observed data highlights three potential SMS zones consisting of 0.2 ohm-m low resistivity embedded into 1 ohm-m sediment.

INTRODUCTION

The marine controlled-source electromagnetic (CSEM) method is a geophysical tool used to remotely map seafloor resistivity structures (Constable, 2010). The CSEM method involves a high-powered electric dipole transmitter towed by a ship in conjunction with electromagnetic (EM) field receivers. Exploration depth is largely determined by the transmitter-receiver separations and the transmitting frequency. CSEM data with large transmitter-receiver separations and low frequencies have been used to elucidate the geology of the oceanic lithosphere (Chave and Cox, 1982; Cox et al., 1986; Evans et al., 1994; MacGregor et al., 1998; Key et al., 2012; Naif et al., 2015; Johansen et al., 2019) and explore deeply buried hydrocarbons (Eidesmo et al., 2002; Yamane et al., 2009; Constable, 2010; Hesthammer et al., 2010; Zhdanov et al., 2014; Myer et al., 2015; Hoversten et al., 2021). CSEM data recorded at relatively short transmitter-receiver separations are sensitive to near-seafloor targets, such as seafloor massive sulfide (SMS) (Haroon et al., 2018; Gehrmann et al., 2019), gas hydrates (Yuan and Edwards, 2000; Schwalenberg et al., 2010; Weitemeyer et al., 2011; Attias et al., 2016; Constable et al., 2016), permafrost (Sherman et al., 2017),

Manuscript received by the Editor 17 May 2021; revised manuscript received 24 January 2022; published ahead of production 29 March 2022; published online 13 May 2022.
[1]Formerly Kyoto University, Department of Urban Management, Kyoto, Japan; Tokyo Institute of Technology, Volcanic Fluid Research Center, Tokyo, Japan; and Japan Agency for Marine-Earth Science and Technology (JAMSTEC), Research Institute for Marine Resources Utilization, Yokosuka, Kanagawa, Japan; presently University of Hyogo, Graduate School of Science, Himeji, Hyogo, Japan. E-mail: ishizu.keiichi.n30@kyoto-u.jp (corresponding author).
[2]Mahidol University, Faculty of Science, Department of Physics, Rajthewee, Bangkok, Thailand and Thailand Center of Excellence in Physics, Commission on Higher Education, Bangkok, Thailand. E-mail: wsiripun@gmail.com.
[3]Kyoto University, Department of Urban Management, Kyoto, Japan and University of Hyogo, Graduate School of Science, Himeji, Hyogo, Japan. E-mail: t.n.goto@sci.u-hyogo.ac.jp.
[4]Kyoto University, Department of Urban Management, Kyoto, Japan. E-mail: koike.katsuaki.5x@kyoto-u.ac.jp.
[5]Japan Agency for Marine-Earth Science and Technology (JAMSTEC), Research Institute for Marine Resources Utilization, Yokosuka, Kanagawa, Japan. E-mail: tkasa@jamstec.go.jp.
[6]Nippon Marine Enterprises, Ltd., Marine Survey Department, Kanagawa, Japan. E-mail: iwamotoh@nme.co.jp.

DOI:10.1190/geo2021-0328.1

and freshwater aquifers (Blatter et al., 2019; Gustafson et al., 2019; Attias et al., 2020; Micallef et al., 2020).

The 3D marine CSEM surveys are useful for mapping complex resistivity structures (Commer and Newman, 2008; Plessix and Mulder, 2008; Abubakar et al., 2009; Sasaki and Meju, 2009; Zhdanov et al., 2014; Morten et al., 2015; Dehiya et al., 2017; Dunham et al., 2018; Meju et al., 2018; Wang et al., 2018; Hoversten et al., 2021). These 3D CSEM surveys have been used to map hydrocarbons by using dozens of ocean-bottom electric (OBE) receivers deployed in a grid pattern and several transmitter towlines (e.g., Newman et al., 2010; Morten et al., 2016). Although completing several transmitter lines may be carried out relatively rapidly when using a ship, the deployments and recovery of OBE receivers are a time-intensive exercise; this is the most cost-demanding aspect. As such, the number of OBE receivers heavily influences the cost of the 3D survey. This study considers SMS exploration, and the horizontal survey scale of SMS is a few kilometers, which is small compared with hydrocarbon surveys of tens of kilometers. If we apply a 3D CSEM survey using a receiver deployment in a grid pattern to map SMS, high survey costs will be incurred due to a large number of receivers despite the small survey size. The cost-effectiveness of the 3D CSEM survey may be increased by omitting redundant OBE receivers and reducing the number of OBE receivers. However, to date, an economical 3D CSEM survey using fewer OBE receivers has not yet been proposed for exploring SMS. This study proposes a cost-effective 3D CSEM survey using fewer receivers than the survey with a receiver deployment in a grid pattern to reduce survey cost and time. This proposed survey only uses a line of OBE receivers in the center of the survey area and several transmitter towlines.

We explore SMS deposits in a hydrothermal area using the proposed CSEM survey. SMS deposits, one of the major near-seafloor targets, are an economical metal resource in the deep sea (Hannington et al., 2011; Murton et al., 2019). These deposits are rich in metals such as copper, tin, zinc, gold, and silver (Herzig and Hannington, 1995; Spagnoli et al., 2016; Komori et al., 2017). SMS deposits have been discovered in hydrothermal areas located near midocean ridges and along the submarine volcanic arc and back-arc spreading centers (Hannington et al., 2011; Boschen et al., 2013; Petersen et al., 2018; Nozaki et al., 2021). In Japan, SMS deposits have been found in the Okinawa Trough (Expedition 331 Scientists, 2010) and the Izu-Ogasawara arc (Iizasa et al., 1999). Recently, the Japan Oil, Gas, and Metals National Corporation has achieved the consecutive lifting of ore and seawater in a state of solid-liquid flow from a depth of 1600 m in the Okinawa Trough for the future development of the SMS deposit (Yamaji et al., 2019).

There is a resistivity contrast between highly conductive SMS and relatively resistive surrounding rocks (Cairns et al., 1996; Von Herzen et al., 1996; Kowalczyk, 2008; Spagnoli et al., 2016; Safipour et al., 2018; Ishizu et al., 2019). Marine CSEM methods are able to detect SMS deposits because of this resistivity contrast. Pilot CSEM surveys at the trans-Atlantic geotraverse (TAG) mounds have found that low-resistivity zones (0.2 ohm-m) are associated with SMS (Cairns et al., 1996), and recent CSEM studies have been able to acquire detailed resistivity distributions of SMS deposits (Constable et al., 2018; Haroon et al., 2018; Müller et al., 2018; Gehrmann et al., 2019). These CSEM studies also reveal that the resistivity distributions of SMS deposits are complex and three-dimensional. This means that a 3D CSEM survey is beneficial in accurately obtaining the distribution of SMS (Haroon et al., 2018).

This study initially describes the proposed 3D CSEM survey and demonstrates the high cost-effectiveness of the proposed survey using synthetic CSEM data. Then, we describe the application of the proposed 3D CSEM survey to explore SMS deposits in the Ieyama hydrothermal area off Okinawa, southwest Japan. The Ieyama hydrothermal area is considered to be a promising location for SMS deposits (Kasaya et al., 2020), and there have been requests to clarify the 3D geometry of SMS deposits to inform the feasibility evaluation of resource development. This study identifies the potential SMS zones using the 3D resistivity structures obtained from CSEM data inversion.

METHODS

Cost-effective 3D marine CSEM survey using fewer OBE receivers

Marine CSEM methods use a deep-towed transmitter to inject a time-varying current into seawater (Chave and Cox, 1982; Constable, 2013). The EM signal diffuses away from the transmitter and travels through the ocean, seafloor, and air, in which it is modified by the conductivity of each medium (Chave, 2009; Constable, 2010; Key, 2012; Mittet and Morten, 2012; Everett and Chave, 2019). The modified EM signal can be recorded by ocean-bottom receivers (Eidesmo et al., 2002; Commer and Newman, 2008; Johansen et al., 2019), towed receivers above the seafloor (Engelmark et al., 2014; Constable et al., 2016; Sherman et al., 2017; Du and Key, 2018), and seafloor-deployed receivers (Evans, 2007; Schwalenberg et al., 2010). This study focuses on a survey configuration with an electric dipole transmitter towed by a ship and OBE receivers (Figure 1a) because a 3D CSEM data set may easily be obtained with this configuration (Commer and Newman, 2008). CSEM surveys with towed transmitters and towed receivers have been widely used in 2D surveys of gas hydrates and SMS deposits (Constable et al., 2016; Gehrmann et al., 2019).

3D marine CSEM surveys have been developed to map hydrocarbons, which are typical CSEM targets and use dozens of OBE receivers deployed on grids and several transmitter towlines (Newman et al., 2010; Morten et al., 2016). Due to the difference in the survey scale of hydrocarbons and SMS, a direct comparison between CSEM surveys for these targets may be difficult. However, because most 3D CSEM surveys reported in the literature use a receiver deployment in a grid pattern and several transmitter towlines (e.g., Newman et al., 2010; Morten et al., 2016), we consider these 3D CSEM surveys to be conventional 3D CSEM surveys for SMS as well. Here, we consider that the survey consists of 35 OBE receivers (five receiver lines) and seven towing lines in an area of 2.5 km × 2.5 km to represent a 3D conventional survey for SMS (Figure 1c). The 35 OBE receivers record data from all transmitting positions (i.e., several inline data sets and the rest as broadside data sets). The spacing between the transmitter towing lines is 300 m, and the spacing between the receiver lines is 400 m.

Our proposed method is a simple one that reduces the receiver array used for hydrocarbon exploration to only line of OBE receivers in the center of the survey area (Figure 1b). The OBE receivers in the center record data from all transmitting positions for the proposed survey (i.e., one inline data set and all of the rest as broadside data sets). We assume that the data set obtained with the proposed survey using a line of OBE receivers has sufficient information to recover the 3D resistivity structures of SMS, whereas the remaining OBE receiver lines can be made redundant. Note that, considering the same number of receivers, there are other receiver placement options

for an economical 3D marine CSEM survey for SMS exploration (e.g., a CSEM survey using staggered receiver placement). We will consider other possible receiver placement options in a future paper.

In the real field example that will be described, we use mobile-type OBE receivers settled on and recovered from the seafloor by a remotely operated vehicle (ROV) in addition to self-popup-type OBE receivers deployed from vessels. Although we use two types of OBE receivers in the field, the approach with fewer receivers also is useful for improving survey efficiency in the CSEM survey mode that we use in the field. We also note that our towline geometry of the transmitter is not similar to that used for commercial CSEM surveys for hydrocarbon explorations. Although this study only considers transmitter towlines parallel to receiver lines and all receivers do not use in-tow and out-tow data, commercial CSEM surveys for hydrocarbon explorations use crosslines of transmitter towing in addition to the parallel lines, and all receivers use in-tow and out-tow data (Newman et al., 2010; Morten et al., 2016).

We briefly compare our survey approach using a towed transmitter and OBE receivers with other CSEM methods that have been used for SMS exploration. Constable et al. (2018) use stationary transmitters deployed on the seafloor and receivers mounted on an autonomous underwater vehicle (AUV). Gehrmann et al. (2019) use towed CSEM receiver of Vulcan (Constable et al., 2016) and towed transmitter. We can consider the AUV-CSEM system in Constable et al. (2018) as a reciprocal version of transmitter and receiver for our system. The transmitter is towed and the receiver is stationary in our system; the receiver is towed and the transmitter is stationary in Constable et al. (2018). Thus, our approach for efficient surveys is applicable for the AUV-CSEM surveys. If we apply our strategy for AUV-CSEM surveys, we use a few stationary transmitters in the center of the survey and several receiver towlines by AUV. It is worth mentioning that the AUV-CSEM system is superior in terms of the speed of SMS exploration. The towed receiver system of Vulcan can obtain a high-resolution data set on a 2D profile (Constable et al., 2016; Gehrmann et al., 2019), and towed receiver data with fixed transmitter-receiver separations (e.g., 100–500 m) are sensitive to shallow structures (Constable et al., 2016). A significant difference between the Vulcan system and our system is that the Vulcan system only uses inline data with fixed transmitter-receiver offset and does not use broadside data. We consider that the broadside data are useful for determining the 3D geometry of the target structures. Recent CSEM surveys have used towed receivers and OBE receivers (Morten et al., 2015; Attias et al., 2018). Towed and OBE receivers can simultaneously measure the response from the transmitter without interference. The combination of towed receiver data and OBE receiver data can improve the resolution of determining shallow and deep structures (Morten et al., 2015; Attias et al., 2018). Therefore, adding towed receivers to the proposed survey would improve further cost-effectiveness because it can improve the resolution to SMS without increasing the survey time. In a future study, we plan to report on the application of the combination of towed and OBE data to SMS exploration.

3D CSEM inversion algorithm

We have developed a new 3D marine CSEM inversion code based on a data-space Occam algorithm. In this section, we describe the 3D CSEM inversion code. Appendix A provides details on the forward modeling using the finite-difference method (FDM) and its validation using a 3D resistivity model. A modified version of this code for the application of offshore-onshore resistivity imaging is reported in Ishizu and Ogawa (2021).

The Occam inversion algorithm, a variant of Gauss-Newton, specifies the minimum norm model with the desired data misfit by automatically adjusting the regularization parameter (Constable et al., 1987). Because of its automatic adjustment of the regularization parameter and the fast convergence, the Occam algorithm has been used for inversion of various EM data (deGroot-Hedlin and Constable, 1990; Siripunvaraporn et al., 2005; Key, 2009, 2016;

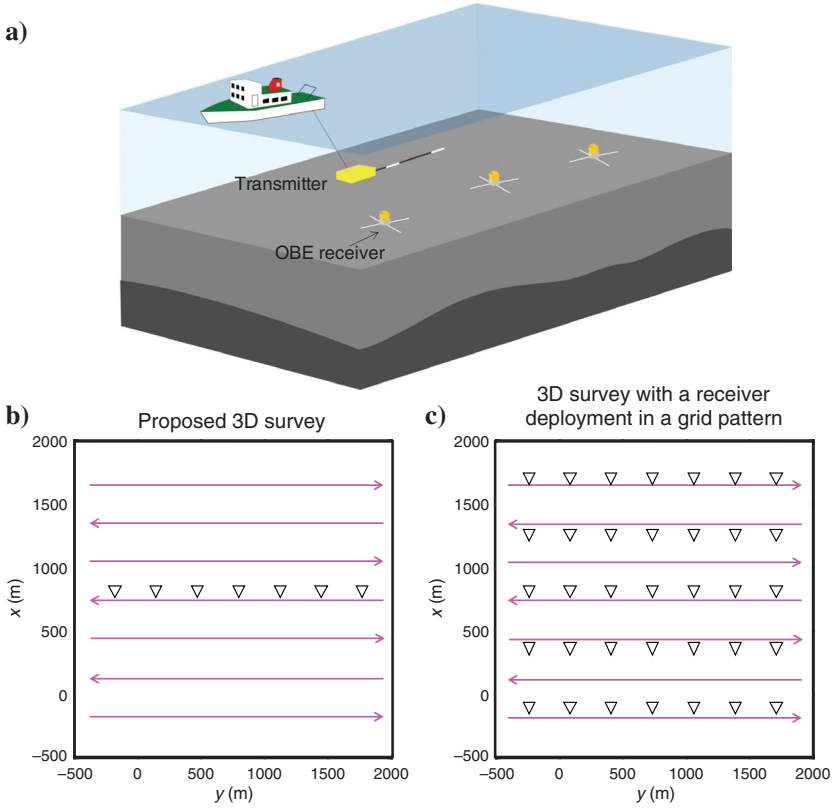

Figure 1. (a) Schematic of a marine CSEM method. We use a CSEM method that involves a towed dipole transmitter and OBE receivers. A pair of transmitter electrodes injects a time-varying current into the seawater. Then, the OBE receivers record the resulting electric signals, which contain information on subseafloor resistivity. Configuration of (b) the proposed 3D CSEM survey and (c) a 3D survey with a receiver deployment in a grid pattern. We refer to a 3D survey with a receiver deployment in a grid pattern as the conventional survey. The spacing between the transmitter towing lines is 300 m for the proposed and conventional surveys. The spacing between the receiver lines for the conventional survey is 400 m. The proposed survey uses only one line of OBE receivers in the center of the survey area. The magenta lines and white triangles represent the transmitter tow lines and OBE receivers, respectively.

Baba et al., 2013) and 3D CSEM data (Zhang and Key, 2016). The Occam inversion algorithm seeks to minimize the functional presented here (Constable et al., 1987):

$$U = (\mathbf{m}-\mathbf{m}_0)^T\mathbf{C}_m^{-1}(\mathbf{m}-\mathbf{m}_0) + \lambda^{-1}\{(\mathbf{d}-\mathbf{F}[\mathbf{m}])^T\mathbf{C}_d^{-1}(\mathbf{d}-\mathbf{F}[\mathbf{m}]) - \chi_*^2\}. \quad (1)$$

In this equation, $\mathbf{m}$ is a vector $\log_{10}\sigma$, $\mathbf{m}_0$ denotes a prior model, $\mathbf{d}$ represents the observed data, $\mathbf{F}[\mathbf{m}]$ signifies the forward modeling response, $\mathbf{C}_m$ is model covariance, $\mathbf{C}_d$ is a data covariance matrix, χ_* represents the desired level of misfit, and λ^{-1} is a Lagrange multiplier. The regularization $\mathbf{C}_m^{-1}$ is defined as the first derivative roughness penalty:

$$\mathbf{C}_m^{-1} = \alpha_x|\partial_x\mathbf{m}|^2 + \alpha_y|\partial_y\mathbf{m}|^2 + \alpha_z|\partial_z\mathbf{m}|^2, \quad (2)$$

where ∂ denotes the finite difference in the model parameter between adjacent blocks (matrix of 1's and -1's) and is independent of the model cell sizes:

$$\partial = \begin{bmatrix} w_1 & & & \mathbf{0} \\ & w_2 & & \\ & & \ddots & \\ \mathbf{0} & & w_{M-1} & \\ & & \cdots & w_M \end{bmatrix} \begin{bmatrix} -1 & 1 & & \mathbf{0} \\ & -1 & 1 & \\ & & \ddots & \\ \mathbf{0} & & -1 & 1 \\ & & \cdots & \mathbf{0} \end{bmatrix}. \quad (3)$$

The α_x, α_y, and α_z are coefficients that affect the relative importance of different components of the first-derivative roughness penalty (Li and Oldenburg, 1996), and w represents penalty weights (Key, 2009). If the relative importance of different components of the roughness penalty is known, α_x, α_y, and α_z can be adjusted. If jumps in resistivity are desired at specific locations, w can be reduced for the corresponding locations (Key, 2009). Because we have little a priori information on the seafloor resistivity structure in this study, we set α_x, α_y, α_z, and w to one.

To minimize U in equation 1, we take the derivative of the objective function with respect to the model and set it to zero. After linearizing an initial model ($\mathbf{m}_k$), the next model $\mathbf{m}_{k+1}$ is expressed by equation 4 for the model-space approach (Constable et al., 1987):

$$[\lambda\mathbf{C}_m^{-1} + \mathbf{J}_k^T\mathbf{C}_d^{-1}\mathbf{J}_k](\mathbf{m}_{k+1}-\mathbf{m}_0) = \mathbf{J}_k^T\mathbf{C}_d^{-1}\hat{\mathbf{d}}_k, \quad (4)$$

where

$$\hat{\mathbf{d}}_k = \mathbf{d} - \mathbf{F}[\mathbf{m}_k] + \mathbf{J}_k(\mathbf{m}_k - \mathbf{m}_0). \quad (5)$$

The dense and symmetric matrix in equation 4 has dimension $M \times M$. Therein, $\mathbf{J}_k$ is the sensitivity matrix (Jacobian) of $N \times M$ at $\mathbf{m}_k$ where M and N, respectively, denote the number of model and data parameters. The Jacobian is obtainable by forward solutions and adjoint solutions (Egbert and Kelbert, 2012). The adjoint solution is obtained by adding the adjoint source to the right side of equation A-2 and solving equation A-2 (Appendix A); this is the usual "reciprocity" trick for the efficient calculation of the Jacobian (Egbert and Kelbert, 2012). Once the matrix $\mathbf{A}$ in equation A-2 is factored using the direct forward solver PARDISO (Schenk and Gärtner, 2004), PARDISO can compute the factored system for multiple right sides inexpensively (Appendix A). Because of the fastness of PARDISO to many right sides, we solve the forward and adjoint solutions as the same right side group in equation A-2. Once the sensitivity matrix is formed, it can be stored and reused for the parameter searching process of λ at each iteration in the Occam inversion algorithm.

The data-space approach (Siripunvaraporn and Egbert, 2000; Siripunvaraporn et al., 2005; Kordy et al., 2016) replaces equation 4 with a linear equation with N unknowns. When equation 4 is left-multiplied by $\mathbf{C}_m$, one obtains

$$\mathbf{m}_{k+1} - \mathbf{m}_0 = \mathbf{C}_m\mathbf{J}_k^T\boldsymbol{\beta}_{k+1}, \quad (6)$$

where $\boldsymbol{\beta}_{k+1}$ is an unknown expansion coefficient vector of the basis functions $\mathbf{C}_m\mathbf{J}_k^T$. The vector $\boldsymbol{\beta}_{k+1}$ is obtained by solving equation 7:

$$(\lambda\mathbf{C}_d + \mathbf{J}_k\mathbf{C}_m\mathbf{J}_k^T)\boldsymbol{\beta}_{k+1} = \hat{\mathbf{d}}_k, \quad (7)$$

The matrix size in equation 7 is $N \times N$. The major difference between equations 4 and 7 is that the dimensions of the system of equations to be solved can be reduced from $M \times M$ in the model-space approach to $N \times N$ in the data-space approach. The data-space approach reduces the computation costs of memory and central processing unit (CPU) time if N is less than M (Siripunvaraporn and Egbert, 2000). For the 3D CSEM method considered here, N is much less than M, resulting in a reduction of the computational costs. The detail of solving the matrix for model update and λ searching algorithm is described in Appendix B.

RESULTS OF APPLICATION TO SYNTHETIC DATA

Synthetic inversion examples using data from four seafloor resistivity models are presented to demonstrate the applicability of the proposed CSEM method to near-seafloor targets (cases I–IV).

CSEM survey and synthetic data settings

The proposed survey used a line of seven OBE receivers in the center of the survey area and seven transmitter towlines (70 transmitting points). The seven OBE receivers recorded data from all transmitting positions (i.e., one inline data set and the rest as broadside data sets). The conventional 3D CSEM survey used five lines of OBE receivers (35 receivers) and seven transmitter towlines (e.g., Newman et al., 2010; Morten et al., 2016). The 35 OBE receivers recorded data from all transmitting positions. The spacing between the transmitter towing lines was 300 m, and the spacing between the receiver lines was 400 m. A horizontal electric dipole (HED) with 28.3 m length was used as the transmitter. The HED used in the transmitter was oriented along the y-direction and towed at 50 m above the seafloor. We considered data with a transmitter-receiver offset >150 m in this study; this offset length was approximately five times the dipole length. The point dipole approximation was valid for data in which the offset of the transmitter and receiver is greater than three to four times the dipole length (Streich and Becken, 2011). Thus, we modeled the source dipole as a point-source dipole to increase the computational efficiency. A point-source dipole also was used as the receiver. Note that x and y cor-

DOI:10.1190/geo2021-0328.1

respond to northing and easting, respectively, and z represents depth below the sea surface.

The models to generate the synthetic CSEM data contained conductive and resistive objects embedded in a 1 ohm-m homogeneous half-space (cases I–IV). In the geologic setting that this study considers, the conductive and resistive objects simulated the SMS deposits and volcanic rocks, respectively. An air layer with a resistivity of 10^8 ohm-m was situated at the top of the model, and the seawater depth with a resistivity of 0.3 ohm-m was 1000 m. CSEM data used in this numerical experiment were generated by forward modeling on a grid of $67 \times 67 \times 68$ cells, including several boundary cells. For horizontal cells, a 50 m grid was used in the interest region. We appended several boundary cells on each side, growing in size at a stretching factor of 2.0. For the vertical grid, fine grids with 20 m spacing were used in the region 1000–1400 m below the sea surface. The grid size increased gradually with distance from the transmitter.

The inversion domain was limited to the interesting seafloor region, excluding boundary cells, sea, and air; this produced $M = 142,175$ unknown model parameters. The starting and prior models for the examples were a homogeneous half-space with a resistivity of 1 ohm-m. The input data set for the inversion used a combination of $\log_{10}$-scaled amplitude and linear-scaled phase of E_y. This combination was able to accelerate convergence in the inversion compared to a combination of real and imaginary electric fields (Wheelock et al., 2015). The component for source-receiver distances exceeding 300 m at frequencies of 0.1 Hz, 0.5 Hz, and 3.0 Hz produced $N = 2844$ and $N = 14,028$ data sets for the proposed and conventional surveys, respectively. In total, 3% Gaussian noise was added to the data in which 0.013 was used for $\log_{10}$-scaled amplitude and 1.72° was used for the phase; an error bar of 3% was used for all data. The target root-mean-square (rms) misfit was set to 1.0. An rms misfit of 1.0 indicated that the average misfit was within the assumed error. The inversion was performed on a computer (@Xeon 3.10 GHz Gold 6254 CPU; Intel Corp.) with 3 TB of random access memory. Solvers of PARDISO, "dgemm," and "dposv" were implemented with 20 OpenMP threads (Appendices A and B). We applied parallel implementation with 70 message passing interface (MPI) processes to the computation of the primary field (Appendix A).

Case I: Anomalies below receiver line

The test for case I considered a model in which a resistor and conductor were embedded immediately below the receiver line in the center of the survey area (Figure 2a). A 0.1 ohm-m conductive and 10 ohm-m resistive object with dimensions of 500 m × 500 m × 200 m were embedded with the respective tops at 1100 m depth. The model grid, survey configuration, error settings, and transmission frequencies were described in the "CSEM survey and synthetic data settings" section.

The rms misfit of the starting model was 10.5 for the data set obtained with the proposed survey. The inversion reached the target rms misfit of 1.0 after three iterations (phase I). Then, two more iterations were conducted to ascertain the minimum norm model with the target rms misfit (phase II). The results demonstrated that the inversion of the data set obtained with the proposed survey sufficiently recovered the positions and resistivity values of both anomalies (Figure 2b) and fit the observed data (Figure 3). The peak resistivity values of the recovered conductor and resistor from the proposed survey were close to their true values (Figure 2h–2j). The tops of both anomalies were clearly distinguishable from the homogeneous half-space. The horizontal shapes of the top parts of both anomalies also were well recovered. The imaged bottom of the anomalies was not as clear as the top; this low resolution of deeper parts is typical for EM exploration (Key, 2016). The target anomalies caused the discrepancy between the computed response from the initial model and the final model (Figure 3). The discrepancy was largest at 3 Hz (Figure 3), indicating that the 3 Hz data are sensitive to anomalies. Thus, adding frequency data of approximately 3 Hz may help to improve the resolution of the inversion algorithm to the top and bottom parts of the anomalies.

For the data set obtained with the conventional survey, the rms misfit of the starting model was 7.2, whereas the inversion obtained a minimum norm model with an rms misfit of 1.0 after five iterations. The inversion results for the conventional survey delineated the conductor and resistor that were similar to the real model (Figure 2e). The peak resistivity values of the recovered conductor and resistor from the conventional survey also were close to the true values (Figure 2h–2j). The peak resistivity value of the recovered resistor from the conventional survey was closer to the true value of 10 ohm-m than that of the recovered resistor from the proposed survey. However, the peak resistivity value of the recovered conductor from the proposed survey was closer to the true value of 0.1 ohm-m than that of the recovered resistor from the conventional survey. However, most features of the inversion result from the proposed survey were indistinguishable from the inversion results of the conventional survey. This result demonstrated that the proposed survey is able to improve the cost-effectiveness of the 3D CSEM surveys for the case I model (Figure 2).

The data sets were $N = 2844$ and $N = 14,028$, with computation times of 06:48:20 and 09:05:47 (hh:mm:ss) for the proposed and conventional surveys, respectively (Table 1). The computation time for the proposed survey was 34% less than the conventional survey. The data-space approach adopted in the inversion algorithm was rapid for a small N, helping to reduce the computation time. The reduction in computational cost was another advantage of the proposed survey.

The proposed survey used one inline data set and the rest as broadside data sets, whereas the conventional survey used several inline data sets and the rest as broadside data sets (Figure 2). The observed inline data for the proposed and conventional surveys exhibited a higher amplitude above the resistor and lower amplitude above the conductor compared to the response from the initial model without the anomalies (Figures 3e, 3f, and 4d). The broadside data also detected the anomalies (Figures 3g, 3h, 4e, and 4f). This broadside data sensitivity indicated that broadside data effectively constrained the anomalies offset from the center receiver line. The broadside data were more sensitive to conductors than resistors (Figures 3g, 3h, 4e, and 4f), indicating that the proposed survey is more effective in the exploration of conductive bodies than resistive bodies. Note that obtaining a data set with this configuration required a 3D inversion analysis. Currently, the 3D inversion code for the CSEM survey has not been distributed among geophysical communities. We plan to make our developed code freely available in the near future.

Case II: Anomalies at different seafloor locations

We considered a model with target anomalies distributed at different seafloor locations (case II: Figure 5a) to demonstrate whether the proposed survey is able to delineate 3D resistivity structures away from

the receiver line. Three 0.1 ohm-m conductive and two 10 ohm-m resistive objects with dimensions of 400 m × 400 m × 200 m were embedded with their respective tops at 1100 m depth. The model grid, survey configuration, error settings, and transmission frequencies were the same as those of case I, as described in the "CSEM survey and synthetic data settings" section.

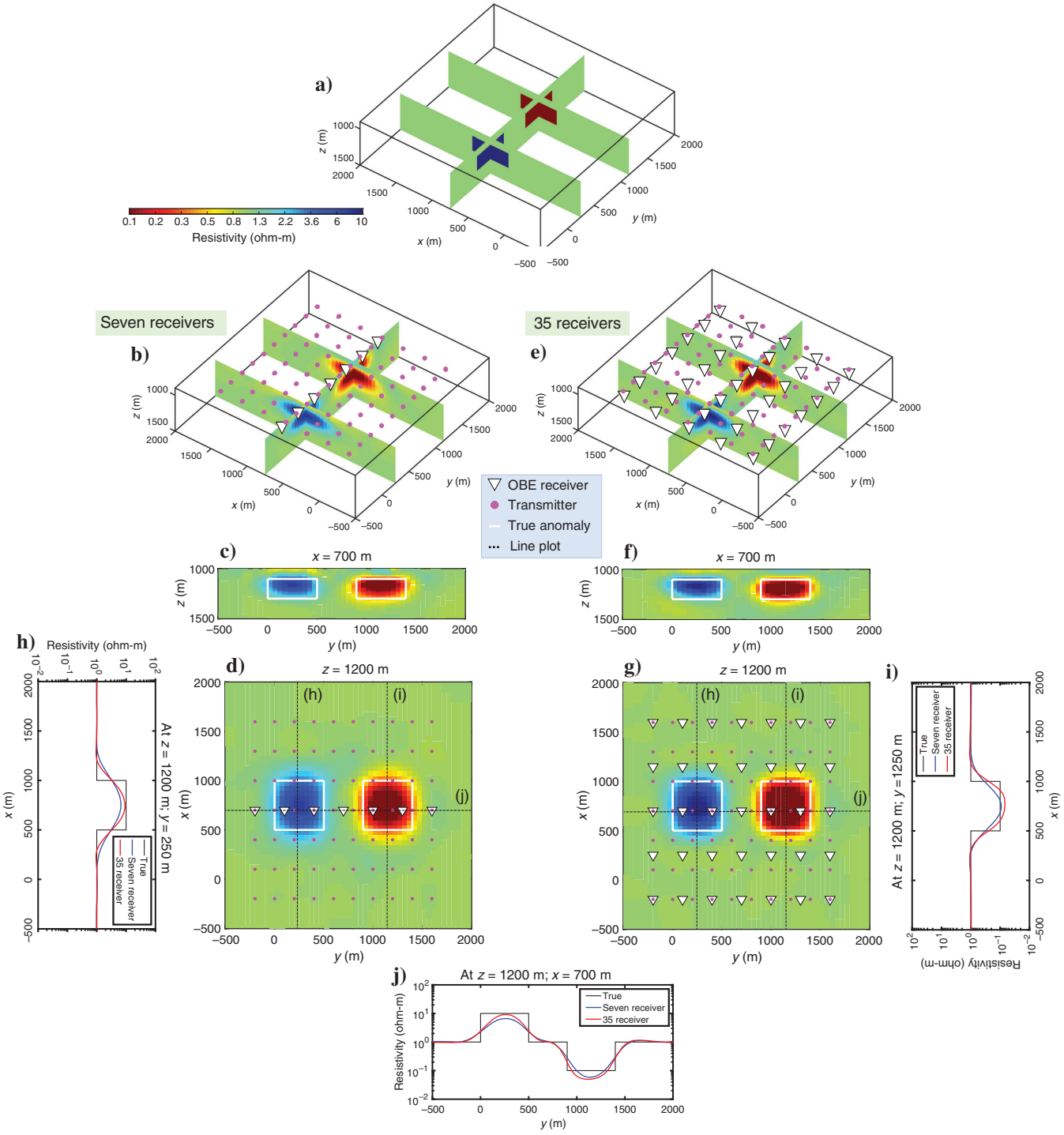

Figure 2. Comparison of the inversion result of the synthetic data set obtained from a proposed survey with the result of the synthetic data set obtained from a conventional survey for a model with anomalies in the survey center (case I). (a) A 3D view of the true model, (b) 3D view, (c) 2D section at $x = 700$ m, (d) 2D section at $z = 1200$ m of the inverted model using the proposed survey (a line of seven OBE receivers in the center of the survey area), (e) 3D view, (f) 2D section at $x = 700$ m, and (g) 2D section at $z = 1200$ m of the inverted model using the conventional survey (35 receivers). The magenta circles and white triangles represent the transmitter and receiver positions, respectively. The white lines mark the outlines of the true anomalies. (h–j) The line plots of models at $z = 1200$ m along the x-axis at $y = 250$ m, the x-axis at $y = 1250$ m, and the y-axis at $x = 700$ m, respectively.

DOI:10.1190/geo2021-0328.1

The rms misfit of the starting model was 9.0 for the data set obtained with the proposed survey. The inversion for the proposed survey obtained the minimum norm model with an rms misfit of 1.0 after four iterations and delineated the anomalies distributed at different seafloor locations, indicating that there was sufficient sensitivity for the area between the transmitter and receiver (Figure 5b). The peak resistivity values of the recovered conductor and resistor from the proposed survey were close to their true values (Figure 5h–5j). The tops of anomalies were clearly distinguishable from the homogeneous half-space. The horizontal shapes of the top parts of anomalies also were well recovered.

For the data set obtained with the conventional survey, the rms misfit of the starting model was 8.5, whereas the inversion obtained a minimum norm model with an rms misfit of 1.0 after six iterations. Similar to the results of case I (Figure 2), the peak resistivity values of the resistors recovered in the conventional survey were closer to the true value of 10 ohm-m than those of the resistors recovered in the proposed survey; the peak resistivity values of the conductors recovered in the proposed survey were closer to the true value of 0.1 ohm-m than those of the conductors recovered in the conventional survey (Figure 5h–5j). However, most features of the inversion result from the proposed survey were indistinguishable from the inversion results of the conventional survey (Figure 5b and 5e). This example demonstrated that the proposed survey is effective in mapping 3D resistivity structures below the receiver line and offset from the receiver line.

Case III: Anomalies at different seafloor locations and different burial depths

The test for case II considered a model in which resistors and conductors were embedded at one depth of $z = 1100$ m (Figure 5b). We considered a model with target anomalies distributed at different seafloor locations and different burial depths (case III: Figure 6a) to demonstrate whether the proposed survey is able to delineate target anomalies at different burial depths distributed below the receiver line and away from the receiver line. Five 0.1 ohm-m conductive objects with dimensions of 400 m × 400 m × 200 m were embedded with their different burial depths. The shallowest burial depth was 0 m (the anomaly is exposed on the seafloor at $z = 1000$ m), whereas the deepest burial depth was 300 m (the anomaly top is at $z = 1300$ m). The model grid, survey configuration, error settings, and transmission frequencies were the same as those of cases I and II, as described in the "CSEM survey and synthetic data settings" section.

The rms misfit of the starting model was 9.1 for the data set obtained with the proposed survey. The inversion for the proposed survey obtained the minimum norm model with an rms misfit of 1.0 after four iterations and delineated the conductors distributed at different seafloor locations and different burial depths (Figure 6c). The conductors were clearly distinguishable from the homogeneous half-space. However, the boundaries of the conductors at burial depths deeper than 200 m were blurred (Figure 6e). The peak resistivity values

Table 1. Comparison of the proposed and conventional surveys for synthetic data in case I (Figure 2).

	Number of OBE receivers	Transmitting points	Data number for inversion	Computation time for inversion (hh:mm:ss)
Proposed survey	7	70	2844	06:48:20
Conventional survey	35	70	14,028	09:05:47

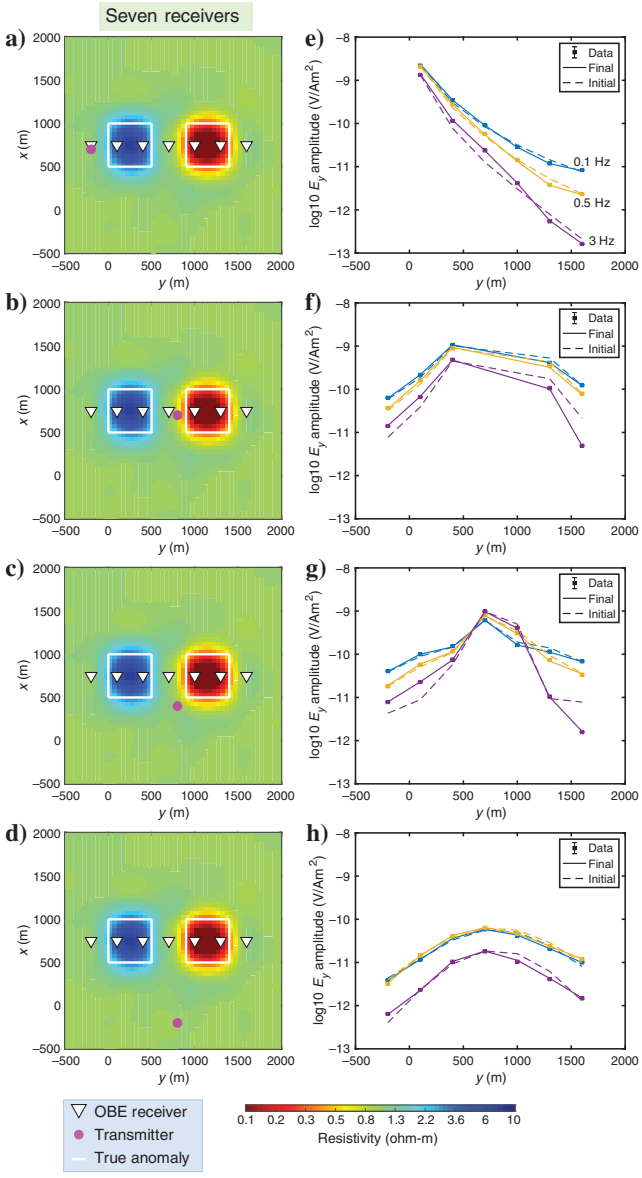

Figure 3. (a–d) Transmitter and receiver positions superimposed on the 2D section at $z = 1200$ m of the inverted model obtained from a proposed survey (case I). The 2D section is the same as Figure 2d. The magenta circles and white triangles represent the transmitter and receiver positions, respectively. The white lines mark the outlines of the true anomaly. (e–h) Observed and predicted data for transmitter and receiver locations in (a–d); (e–h) are for (a–d), respectively. Points with error bars, solid lines, and dashed lines represent observed data, predicted data from the final model, and predicted data from the initial model, respectively. The blue, yellow, and purple represent 0.1 Hz, 0.5 Hz, and 3.0 Hz, respectively. The initial model consists of three layers: a highly resistive air layer (10^8 ohm-m), a seawater layer of constant resistivity (0.3 ohm-m), and a homogeneous seafloor (1 ohm-m).

of the recovered conductors at a burial depth of 200 m and away from the survey center (1000 m < x < 1400 m and 900 m < y < 1300 m), at a burial depth of 300 m and in the survey center (500 m < x < 900 m and 500 m < y < 900 m), and at a burial depth of 300 m and away from the survey center (1000 m < x < 1400 m and 100 m < y < 500 m) were 0.23 ohm-m, 0.32 ohm-m, and 0.4 ohm-m, respectively (Figure 6i–6l).

For the data set obtained with the conventional survey, the rms misfit of the starting model was 12.1, whereas the inversion obtained a minimum norm model with an rms misfit of 1.0 after seven iterations. The inversion for the conventional survey delineated the anomalies distributed at various seafloor locations and different burial depths (Figure 6f). For shallow conductors with burial depths shallower than 200 m, most features of the inversion result from the conventional survey were indistinguishable from the inversion result of the proposed survey (Figure 6). The peak resistivity values of the recovered conductors for the conventional survey at a burial depth of 200 m and away from the survey center (1000 m < x < 1400 m and 900 m < y < 1300 m), at a burial depth of 300 m and in the survey center (500 m < x < 900 m and 500 m < y < 900 m), and at a burial depth of 300 m and away from the survey center (1000 m < x < 1400 m and 100 m < y < 500 m) were 0.08 ohm-m, 0.09 ohm-m, and 0.23 ohm-m, respectively (Figure 6i–6l). The peak resistivity values were closer to the true values compared with those from the proposed survey. The boundaries of conductors at burial depths deeper than 200 m were better reproduced than those from the proposed survey (Figure 6h). Although the proposed and the conventional surveys delineated the deep bodies near the CSEM detection limit, the conventional survey obtained better performance for recovering the deep bodies than the proposed survey. This example demonstrated that the optimal placement of transmitters and receivers depends on the problem.

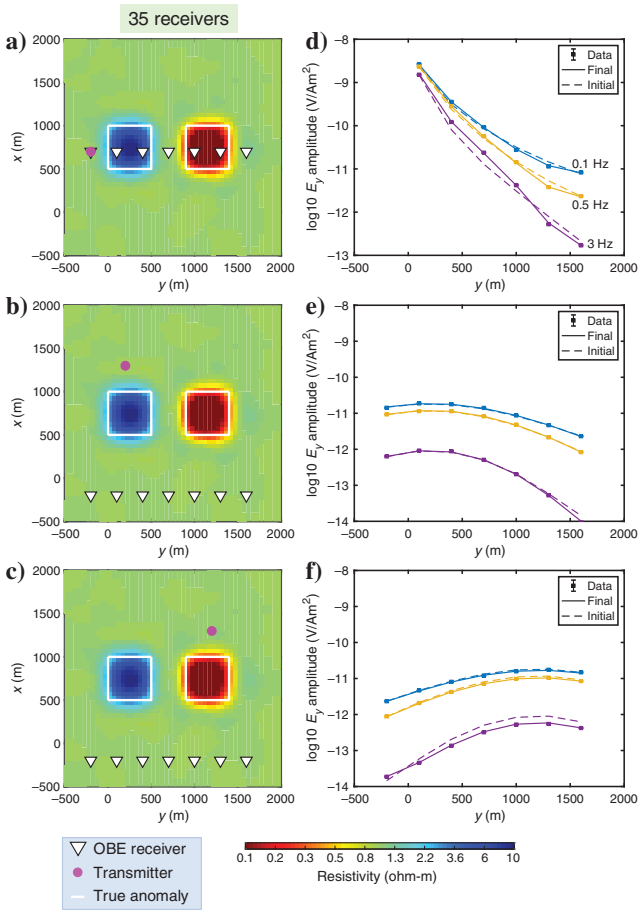

Figure 4. (a–c) Transmitter and receiver positions superimposed on the 2D section at z = 1200 m of the inverted model obtained from a conventional survey (case I). The 2D section is the same, as shown in Figure 2g. (d–f) Observed and predicted data for transmitter and receiver locations in (a–c); (d–f) are for (a–c), respectively. The rest of the explanation is the same as shown in Figure 3.

Case IV: Realistic SMS model and realistic noise

This test considered a more realistic SMS model (case IV: Figure 7a). Five conductive objects simulating the SMS deposit were considered exposed on the seafloor (Figure 7b). Two 0.2 ohm-m conductive objects with dimensions of 400 m × 400 m × 50 m, a 0.2 ohm-m conductive object with dimensions of 400 m × 400 m × 100 m, a 0.2 ohm-m conductive object with dimensions of 300 m × 300 m × 50 m, and a 0.3 ohm-m conductive object with dimensions of 300 m × 300 m × 50 m were exposed on the seafloor. These conductive objects of SMS deposit were based on the inversion result of our field data (which will be shown in the next section) and SMS resistivity models reported by recent electrical and EM studies. These studies have reported the resistivity of SMS to be between 0.1 ohm-m and 0.3 ohm-m, with a horizontal scale of 100–600 m and thickness of 30–70 m (Constable et al., 2018; Haroon et al., 2018; Müller et al., 2018; Gehrmann et al., 2019; Ishizu et al., 2019).

The previous tests (cases I–III) used 3% Gaussian noise for all synthetic data. However, data with short offsets of transmitter and receiver will be affected by position measurement errors of receivers and transmitter, and the noise floor of receivers will influence data with the large offsets (Myer et al., 2012; Gehrmann et al., 2020). In this test of case IV, we considered Gaussian random noise with the noise level predicted by our field data example in the Ieyama hydrothermal area. To consider the noise level depending on the transmitter and receiver separations in field observations, the data from receiver Rx1 at a frequency of 0.125 Hz in the field data example (which will be shown in the next section) were divided into four sections: the transmitter and receiver separations of <500 m, 500–1000 m, 1000–1500 m, and >1500 m. The average error bar for the divided data for the transmitter and receiver separations of <500 m, 500–1000 m, 1000–1500 m, and >1500 m was 8%, 5%, 10%, and 15%, respectively. We added Gaussian random noise with a noise level of 8%, 5%, 10%, and 15% to the synthetic data with transmitter and receiver separations of <500 m, 500–1000 m, 1000–1500 m, and >1500 m, respectively. The noise floor of the receiver Rx1 was approximately 10^{-12} (V/Am^2). We considered this noise floor and discarded the synthetic data smaller than the noise floor from the analysis. Our actual data in the field lacked phase data. Therefore, we only considered the amplitude data in this test.

The model grids for horizontal directions were the same as the previous tests (cases I–III), but for the vertical grid, we used 10 m size for z = 1000−1100 m. Survey configuration also was the same as the previous tests (cases I–III), but transmitting spacing was 50 m based on our field survey. The E_y component with transmitter-receiver distances >150 m at frequencies of 0.1 Hz, 0.5 Hz, and 3.0 Hz produced an N = 7122 data set and N = 34,934 for the proposed survey and conventional survey, respectively. We set the error bars for data with transmitter and receiver separations

of <500 m, 500–1000 m, 1000–1500 m, and >1500 m to 8%, 5%, 10%, and 15%, respectively. These error bars were the same as the added noise level.

The rms misfit of the starting model was 3.3 for the data set obtained using the proposed survey with the realistic noise. The inversion for the proposed survey with the realistic noise obtained the

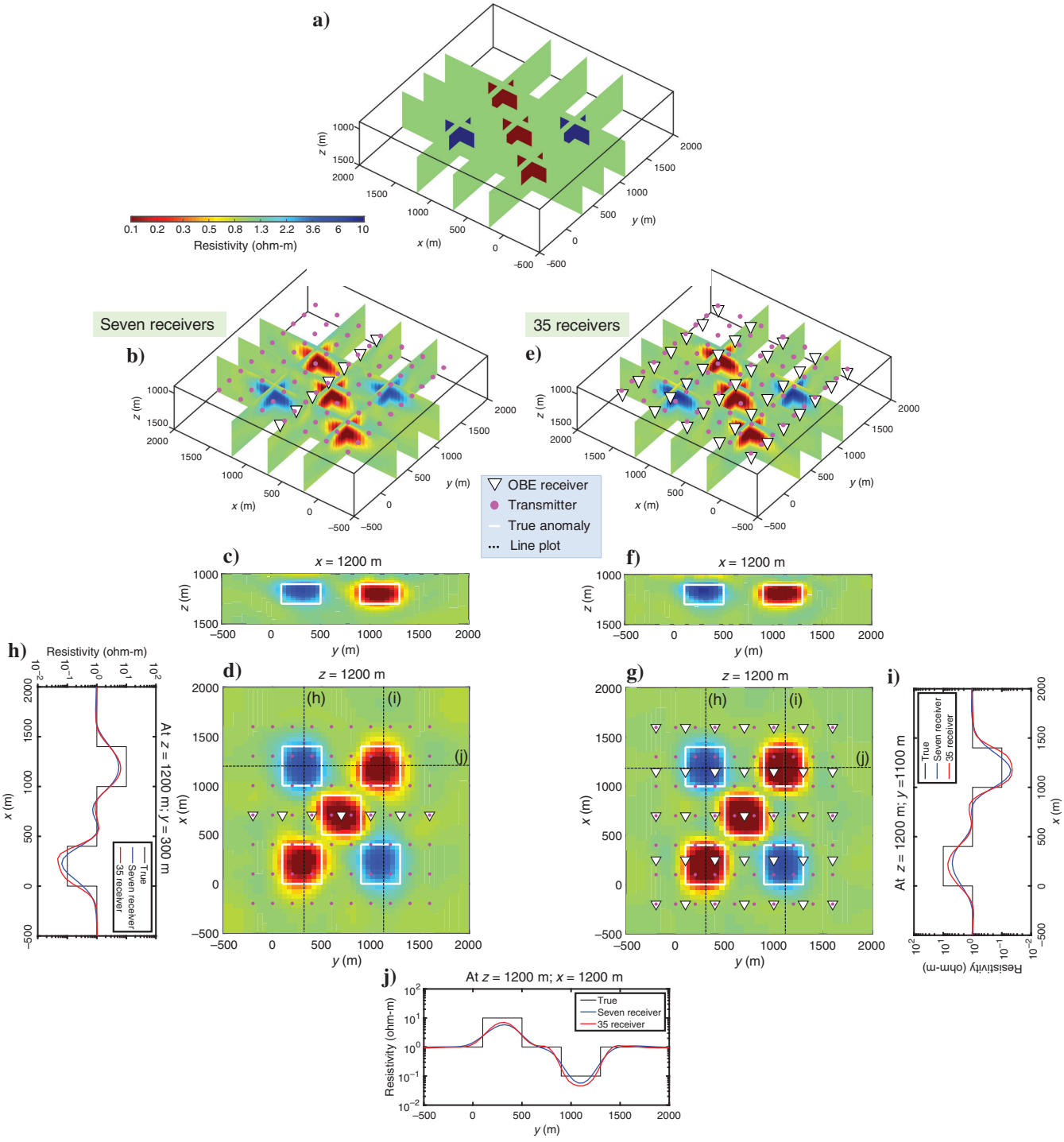

Figure 5. Comparison of the inversion result of the synthetic data set obtained from a proposed survey with the result of the synthetic data set obtained from a conventional survey for a model with anomalies distributed at different seafloor locations (case II). (a) A 3D view of the true model, (b) 3D view, (c) 2D section at $x = 1200$ m, (d) 2D section at $z = 1200$ m of the inverted model using the proposed survey (seven receivers), (e) 3D view, (f) 2D section at $x = 1200$ m, and (g) 2D section at $z = 1200$ m of the inverted model using the conventional survey (35 receivers). (h–j) The line plots of models at $z = 1200$ m along the x-axis at $y = 300$ m, the x-axis at $y = 1100$ m, and the y-axis at $x = 1200$ m, respectively. The rest of the explanation is the same as in Figure 2.

DOI:10.1190/geo2021-0328.1

DOI:10.1190/geo2021-0328.1

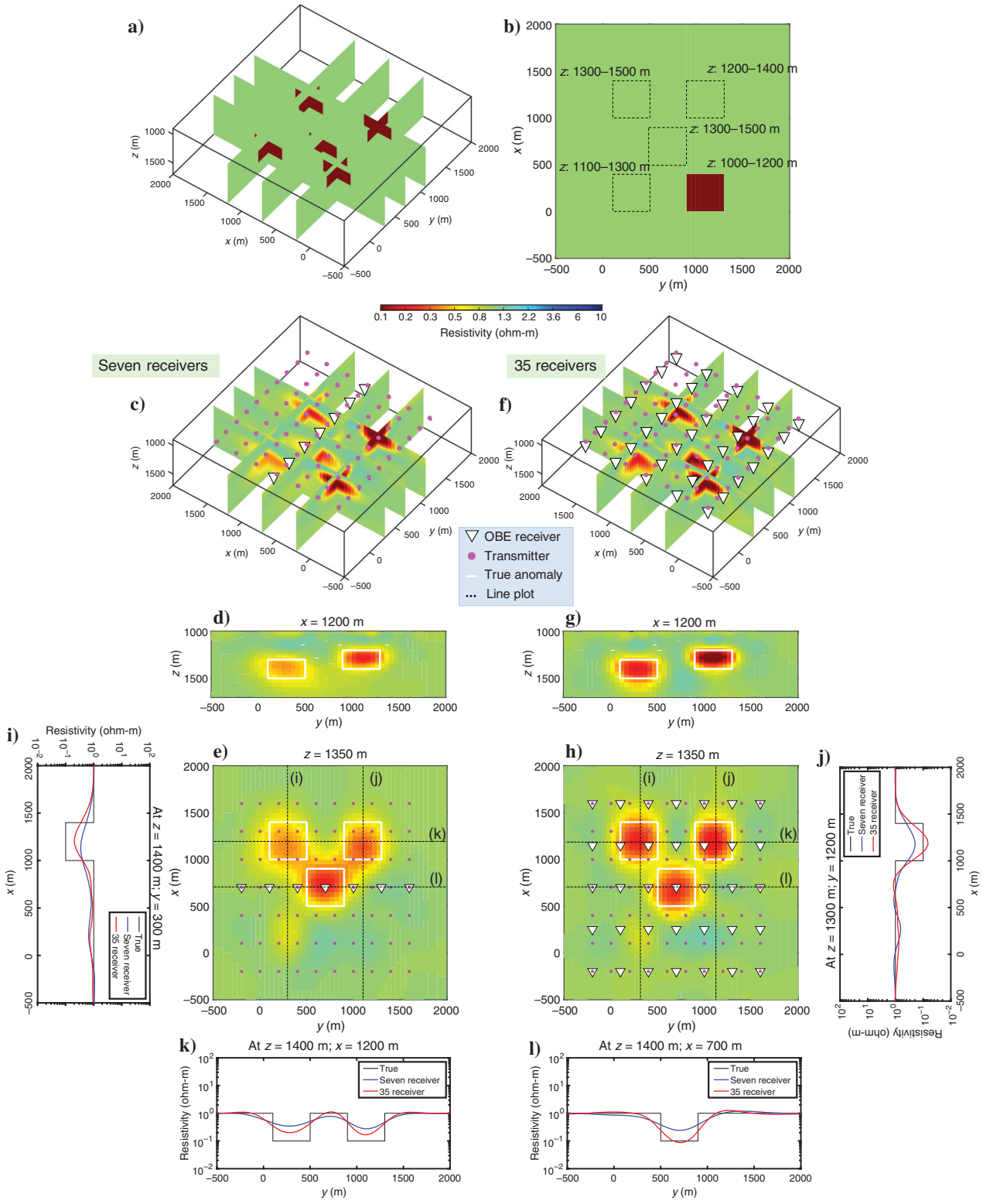

Figure 6. Comparison of the inversion result of the synthetic data set obtained from a proposed survey with the result of the synthetic data set obtained from a conventional survey for a model with anomalies distributed at different depths (case III). (a) A 3D view, (b) 2D section at $z = 1000$ m of the true model, (c) 3D view, (d) 2D section at $x = 1200$ m, (e) 2D section at $z = 1350$ m of the inverted model using the proposed survey (seven receivers), (f) 3D view, (g) 2D section at $x = 1200$ m, and (h) 2D section at $z = 1350$ m of the inverted model using the conventional survey (35 receivers). (i–l) The line plot of models at $z = 1400$ m along the x-axis at $y = 300$ m, at $z = 1300$ m along the x-axis at $y = 1200$ m, at $z = 1400$ m along the y-axis at $x = 1200$ m, and at $z = 1400$ m along the y-axis at $x = 700$ m, respectively. The rest of the explanation is the same as in Figure 2.

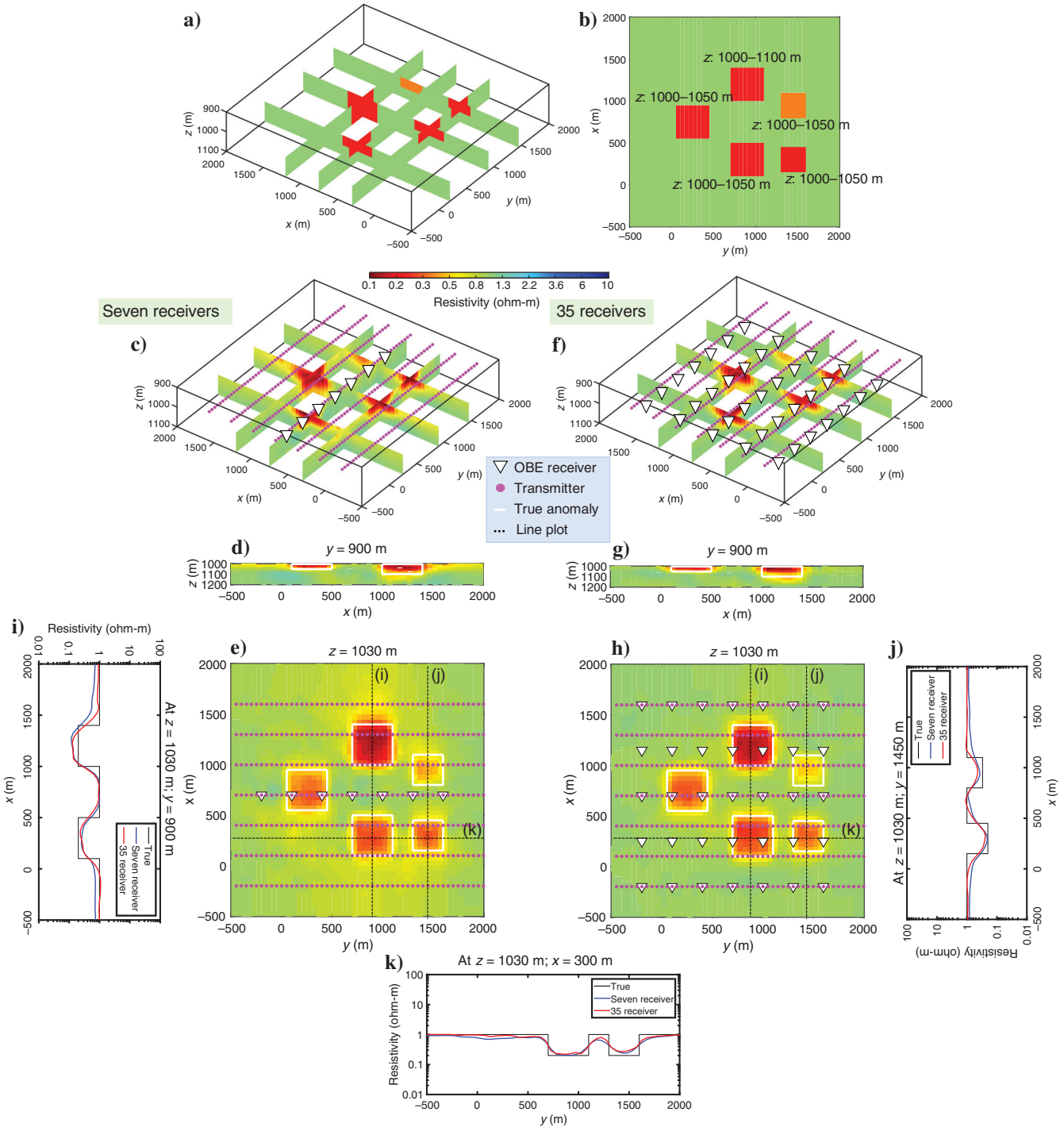

Figure 7. Comparison of the inversion result of the synthetic data set obtained from a proposed survey with the result of the synthetic data set obtained from a conventional survey for a realistic SMS model (case IV). We have added Gaussian random noise with the noise level estimated by the actual field data from the Ieyama hydrothermal area shown in Figure 10 to the synthetic data set to carry out a realistic test (the added noise levels are 8%, 5%, 10%, and 15% for transmitter and receiver separations of <500 m, 500–1000 m, 1000–1500 m, and >1500 m, respectively). (a) A 3D view, (b) 2D section at $z = 1000$ m of the true model, (c) 3D view, (d) 2D section at $y = 900$ m, (e) 2D section at $z = 1030$ m of the inverted model using the proposed survey (seven receivers), (f) 3D view, (g) 2D section at $y = 900$ m, and (h) 2D section at $z = 1030$ m of the inverted model using the conventional survey (35 receivers). (i–k) The line plot of models at $z = 1030$ m along the x-axis at $y = 900$ m, along the x-axis at $y = 1450$ m, and along the y-axis at $x = 300$ m, respectively. The rest of the explanation is the same as in Figure 2.

minimum norm model with an rms misfit of 1.0 after five iterations and delineated the SMS deposits at different seafloor locations and different sizes (Figure 7c). Recovered SMS deposits for the proposed survey with the realistic noise were clearly distinguishable from the homogeneous half-space. The peak resistivity values of the recovered SMS deposits were close to the true values (Figure 7i–7k). The presence of 0.6 ohm-m artifacts at 1300 m $< x <$ 1800 m and 700 m $< y <$ 1100 m was confirmed by the inversion results of the proposed study with the realistic noise. Such artifacts were not recovered in resistivity models in cases I–III for the proposed survey, suggesting that the large error for long-offset data resulted in the artifacts.

For the data set obtained using the conventional survey with the realistic noise, the rms misfit of the starting model was 2.6, whereas the inversion obtained a minimum norm model with an rms misfit of 1.0 after four iterations. The inversion for the conventional survey with the realistic noise also delineated the SMS deposits at different seafloor locations and different sizes (Figure 7f). Most features of the inversion result from the conventional survey were indistinguishable from the inversion results of the proposed survey except for the 0.6 ohm-m artifacts at 1300 m $< x <$ 1800 m and 700 m $< y <$ 1100 m (Figure 7). The inversion for the conventional survey did not recover artifacts, whereas the inversion for the proposed survey recovered 0.6 ohm-m artifacts. However, 0.6 ohm-m artifacts may not be interpreted as SMS because such high-resistivity SMS deposits have not been reported. Thus, the difference between the proposed survey and the conventional survey was not important for SMS exploration.

We also considered a test in which the data were obtained with a 3% error at all offsets of the transmitter and receiver. This test investigated the benefits of obtaining good quality data at all offsets in SMS exploration. The rms misfits of the starting model were 6.9 and 5.6 for data sets obtained using the proposed and the conventional surveys for 3% Gaussian noise, respectively. The inversion of both data sets obtained the minimum norm model with an rms misfit of 1.0 after four iterations. Most features of the inversion result of the proposed survey with 3% Gaussian noise were indistinguishable from the inversion result of the proposed survey with the realistic noise (Figure 8). The resistivity values of artifacts at 1300 m $< x <$ 1800 m and 700 m $< y <$ 1100 m were 0.75 ohm-m for the proposed survey with 3% error and 0.6 ohm-m for the proposed survey with the realistic noise. However, the resistivity difference between the recovered artifacts was not important for SMS exploration because 0.6 ohm-m and 0.75 ohm-m resistivity structures have not been interpreted as SMS. The peak resistivity values of recovered SMS models for four data sets (the proposed survey with realistic noise, the proposed survey with 3% noise, the conventional survey with realistic noise, and the conventional survey with 3% noise) were similar (Figure 8m). This result indicated that, for the SMS model, the proposed survey with realistic noise had performance similar to the conventional survey with 3% errors.

Large noises in the long-offset data (i.e., 15% for data of transmitter and receiver separations of >1500 m) led to poor constraint to target structures away from the receiver line. As a result, the inversion for the proposed survey with the realistic noise imaged artifacts at 1300 m $< x <$ 1800 m and 700 m $< y <$ 1100 m (Figure 7c). In addition, most of the data with transmitter and receiver separations >2 km at a frequency of 3 Hz were less than the noise floor of 10^{-12} $(\mathrm{V/Am^2})$. This indicated that our proposed survey using a line of OBE receivers in the center of the survey area is effective for exploring SMS deposits located within 2 km from the receiver line, and the proposed survey requires a new line of receivers to explore SMS deposits located more than 2 km away from the center receiver line. We also discussed where to place the receiver line in our proposed survey. In our approach, we considered placing the receiver line in the center of the survey area (cases I–IV). If the receiver line were placed in the center of the survey area, our coverage area would be 4 km (i.e., 2 km on one side from the line and 2 km on the other side from the line). However, if we placed the receiver line at the edge of the survey area, the coverage area would be only 2 km from the edge. Therefore, we concluded that placing the receiver line in the center of the survey area is optimal for increasing the coverage area of the proposed survey.

RESULTS AND DISCUSSION OF APPLICATION TO AN SMS AREA

This section describes the application of the proposed 3D CSEM survey to explore SMS deposits. We have collected CSEM survey data in the Ieyama hydrothermal area off Okinawa, southwest Japan, from 6 to 11 October 2017, using the research vessel "Kaimei" from the Japan Agency for Marine-Earth Science and Technology (Figure 9). The proposed survey uses a line of six OBE receivers in the survey center and three transmitter towlines. This survey aims to identify and delineate SMS deposits in the Ieyama hydrothermal area.

Study area

The Okinawa Trough is an active back-arc basin of the Ryukyu arc-trench system, where the Philippine Sea plate is subducting under the Eurasian plate. The Okinawa Trough is considered to be experiencing the initial stage of continental rifting (Letouzey and Kimura, 1986). High heat flow occurs across the entire basin in the mid-Okinawa Trough due to magma intrusion (Ishibashi et al., 2015). Because the hydrothermal activity was first discovered in the Izena area, several seafloor hydrothermal areas have been identified in the mid-Okinawa Trough (Ishibashi et al., 2015). Seafloor drilling has identified SMS zones in the Izena and Iheya hydrothermal areas (Expedition 331 Scientists, 2010; Ishibashi et al., 2015). The Ieyama hydrothermal area is a newly discovered hydrothermal area in the mid-Okinawa Trough and is expected to contain SMS deposits (Kasaya et al., 2020). However, because this hydrothermal area was discovered recently, there is a scarcity of available geologic information for this area.

There are depressions in the Ieyama hydrothermal area (Kasaya et al., 2020), one of which is shown in Figure 9b (at a water depth of 1100 m and at $x = 800$ m and $y = 900$ m), and its horizontal size is 1.5 km × 1.5 km. Faults and hydrothermal activities that can contribute to SMS formation are frequently developed in seafloor depressions (Kasaya et al., 2020). Thus, we consider depressions to be an important structure for SMS formation. In fact, an AUV has identified clusters of hydrothermal plumes west and northeast of the depression center (Kasaya et al., 2020). Video inspection conducted using ROV has identified mound structures west of the depression center (Kasaya et al., 2020). Mounds overlapping with hydrothermal plumes have been hydrothermally active; hydrothermal activity has not been observed in mounds without hydrothermal plumes (Kasaya et al., 2020). A strong self-potential (SP) anomaly has been

observed in the hydrothermally inactive mounds using an AUV (Kasaya et al., 2020). The obtained SP anomaly is "negative" relative to the surroundings, and the diameter of the anomalous area is 250 m (Kasaya et al., 2020). The negative SP area and clusters of hydrothermal plumes do not overlap with each other. This positional discrepancy suggests that the SP anomaly was generated by subseafloor structures, as opposed to the hydrothermal chemical anomaly in seawater (Kasaya et al., 2020). Previous studies conducted in other hydrothermal areas with documented SMS deposits suggest that negative SP anomalies are associated with the seafloor and subsurface massive sulfides (Kawada and Kasaya, 2017, 2018; Safipour et al., 2017; Constable et al., 2018; Zhu et al., 2020). The observed features indicate that SMS deposits are likely to exist in the Ieyama hydrothermal area.

Observed CSEM data

The CSEM survey used a towed dipole transmitter and OBE receiver (Figure 1). A deep-towed marine EM system (MEMSYS) (Kasaya et al., 2019) repeatedly transmitted a cycle of artificial electric current in seawater using a 28.3 m horizontal dipole antenna. Here, a cycle referred to the fundamental base transmitter waveform. A square wave with a frequency of 0.125 Hz (total length of 8 s) and amplitude of approximately ± 60 A was used as the waveform of the current. The Fourier series representation of the square wave gave a coefficient of $4/\pi$ at a fundamental frequency of 0.125 Hz. Thus, the current at the fundamental frequency of 0.125 Hz was 76.4 A ($4/\pi \times 60$ A), and its dipole moment was 2.16 kAm (76.4 A × 28.3 m). The transmitter was switched off

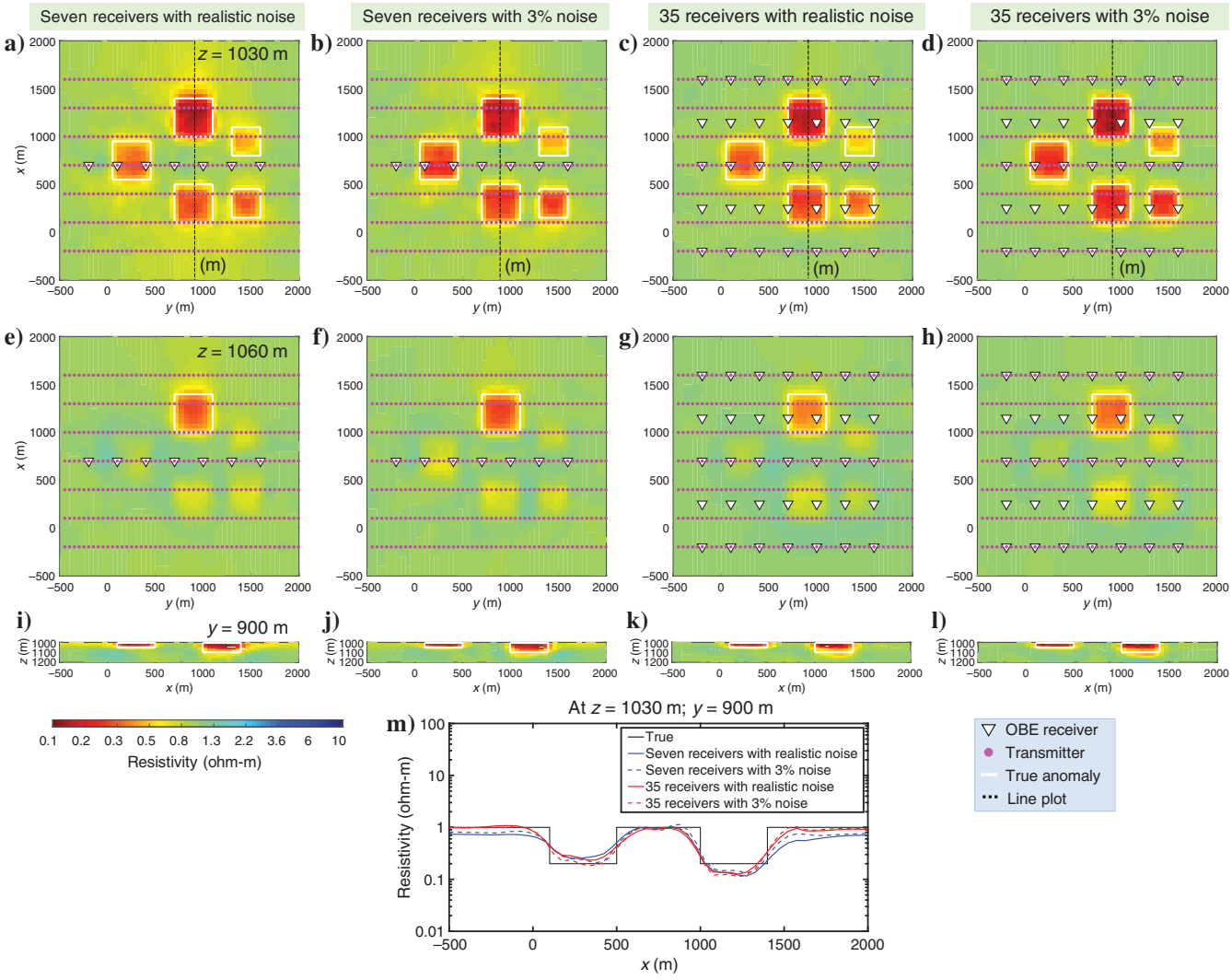

Figure 8. Comparison of the inversion result of synthetic data sets obtained from different survey arrays and different noise levels for case IV (Figure 7). (a–d) The 2D sections at $z = 1030$ m, (e–h) 2D sections at $z = 1060$ m, and (i–l) 2D sections at $y = 900$ m of inverted models. Left and center-left panels are for the inversion results of synthetic data sets obtained from a proposed survey with the addition of realistic noise and 3% noise, respectively. Center-right and right panels are for the inversion results of synthetic data sets obtained from a conventional survey with the addition of realistic noise and 3% noise, respectively. Models in left and center-right panels are the same as models shown in Figure 7c and 7f, respectively. For the realistic noise case, we have added Gaussian random noise with a noise level of 8%, 5%, 10%, and 15% to the synthetic data with transmitter and receiver separations of <500 m, 500–1000 m, 1000–1500 m, and >1500 m, respectively. (m) The line plots of models at $z = 1030$ m along the x-axis at $y = 900$ m. The rest of the explanation is the same as in Figure 2.

DOI:10.1190/geo2021-0328.1

for 12 s after every cycle of the square wave; this off-time was due to our system limitation. Our system was originally developed for a direct current resistivity survey (Ishizu et al., 2019). We used this system for the CSEM survey in the Ieyama hydrothermal area. Thus, for the data set used in this study, the transmitter was switched off after transmitting each current waveform and the frequency of the transmitting waveform was low. Note that the latest version of this system that was improved after this Ieyama survey can repeatedly transmit waveforms without off-time to increase the number of stacks. We used a supershort baseline (SSBL) acoustic navigation system and two acoustic transponders to monitor the transmitter positions. One transponder was attached to the towed transmitter, and the other was attached to the tail of the towed cable. The towed height from the seafloor was monitored by an acoustic altimeter attached to the towed system, and it was maintained at 20–60 m, depending on the topography below the system.

Six OBE receivers, which are modified versions of the instrument by Kasaya and Goto (2009), measured the electric fields at a sampling rate of 1 kHz. Four of these receivers were self-popup-types deployed from vessels (Rx 1, 3, 5, and 6 shown in Figure 9), whereas the remaining two were mobile-type (Rx 2 and 4 shown in Figure 9); the latter was settled on and recovered from the seafloor by the ROV. Each OBE receiver measured the horizontal electric fields using Ag/AgCl electrodes attached to the extended arms. The electric dipole lengths were 4.4 m for the four self-popup OBE receivers and 1.4 m for the mobile-type OBE receivers. We used the same gain for the self-popup and mobile receivers. Acoustic transponders were attached to the four self-popup OBE receivers, and the SSBL system measured the seafloor positions of the four OBE receivers (Figure 9b). In the deployment of our self-popup type OBE receivers, we stopped the ship at the position in which the receiver was dropped, waited for the receiver to land on the seafloor, and measured the receiver position on the seafloor immediately after deployment rather than during the tow. We then moved to the next receiver drop position and repeated the same process. The seafloor positions of the two mobile OBE receivers were determined using a Doppler velocity log navigation for ROV. The sink rate of the self-popup receivers was approximately 50 m/ min, and it took approximately 20 min for the self-popup-type receivers to travel from the sea surface to the seafloor at a sea depth of 1000 m in this field. The sink rate of the ROV with the mobile receivers also was approximately 50 m/min, and it also took approximately 20 min for the ROV to travel from the sea surface to the seafloor. After the ROV landed on the seabed, placing an OBE receiver from the ROV cage on the seafloor took a few minutes. Magnetometers were installed on the OBE receivers to measure the sensor direction.

The frequency-domain transfer function was converted from time-series voltage data recorded at each OBE receiver using a robust processing scheme (Myer et al., 2011). Data were fast Fourier transformed within an 8 s window corresponding precisely to one waveform of length. The electric field (voltage divided by the receiver dipole length) recorded at the OBE receiver was normalized by the transmitted source dipole moment. The data were stacked with each stacking window of 68 s (32 s: four cycles of 8 s square waves

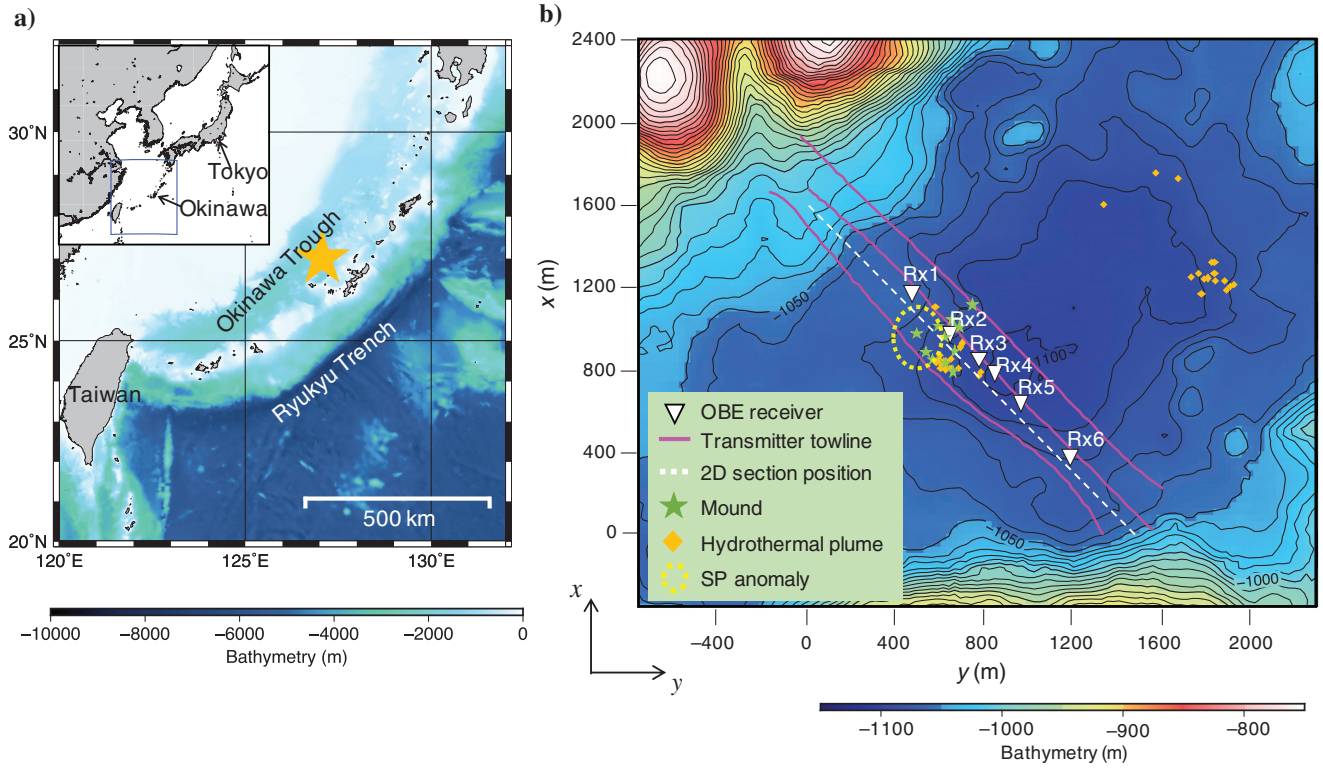

Figure 9. (a) Map of the study area. The yellow star shows the location of the Ieyama hydrothermal area, Okinawa Trough, southwestern Japan. (b) Bathymetric map overlain with the OBE deployment locations (the white triangles), three tow lines (the magenta lines), mounds (the green stars), hydrothermal plumes (the orange rhombus), and SP anomaly area (the dashed yellow lines). The hydrothermal plume and SP data have been obtained using an AUV (Kasaya et al., 2020). For this study, *x* and *y* correspond to northing and easting, respectively. The dashed white line (line 1) represents the 2D section position of the resistivity model shown in Figure 13.

and 36 s: three times of 12 s transmitter off), corresponding to a sample interval of approximately 45 m with the horizontal movement of MEMSYS. The stacked transfer functions of the CSEM data were then rotated into E_x (north component) and E_y (east component), using the dipole orientation recorded by the magnetic field sensors (Figure 10). The error bars in the data were set to their standard deviations estimated by this stacking. Noisy data in which the error bar exceeded 50% were removed for further inversion analysis. Data with a transmitter-receiver offset <150 m also were removed because of navigation errors. Because the receiver noise floors of the self-popup and mobile receivers were approximately 10^{-12} and 10^{-11} $(\mathrm{V/Am^2})$, respectively, the maximum offsets for the data used in the inverse analysis were 2 km and 1.5 km for the self-popup and mobile receivers, respectively. The input data of the inversion analysis were the $\log_{10}$-scaled amplitudes of E_x and E_y at three frequencies of 0.125 Hz, 0.375 Hz, and 0.625 Hz. The phase data were not used because they had been subject to drift caused by nonlinear timing errors. As a result, the data number (N) for inversion analysis was 3833.

Inversion results

The inversion was applied to the processed CSEM data with a 5% minimum error setting. This minimum error setting of 5% changed all error bars for data less than 5% to 5%. We used this minimum error setting of 5% to prevent overfitting against systematic noise in the data. A simple starting model consisted of a highly resistive air layer (10^8 ohm-m), five laterally stratified seawater layers (ranging between 0.200 and 0.304 ohm-m), and a homogeneous seafloor (1 ohm-m). The seawater resistivity values were derived from the seawater resistivity measured using a conductivity-temperature-depth sensor attached to MEMSYS. The model was divided into a grid of $67 \times 67 \times 66$ cells, including several boundary cells. For horizontal cells, a 50 m grid was used in the region of interest, and a 10 m grid was used between 950 m and 1250 m depth below the sea surface for the vertical grid. The seafloor topography was approximated as the stair-step shape of the FDM grid. This approximation was supported by a comparison with the true seafloor topography as the stair-step

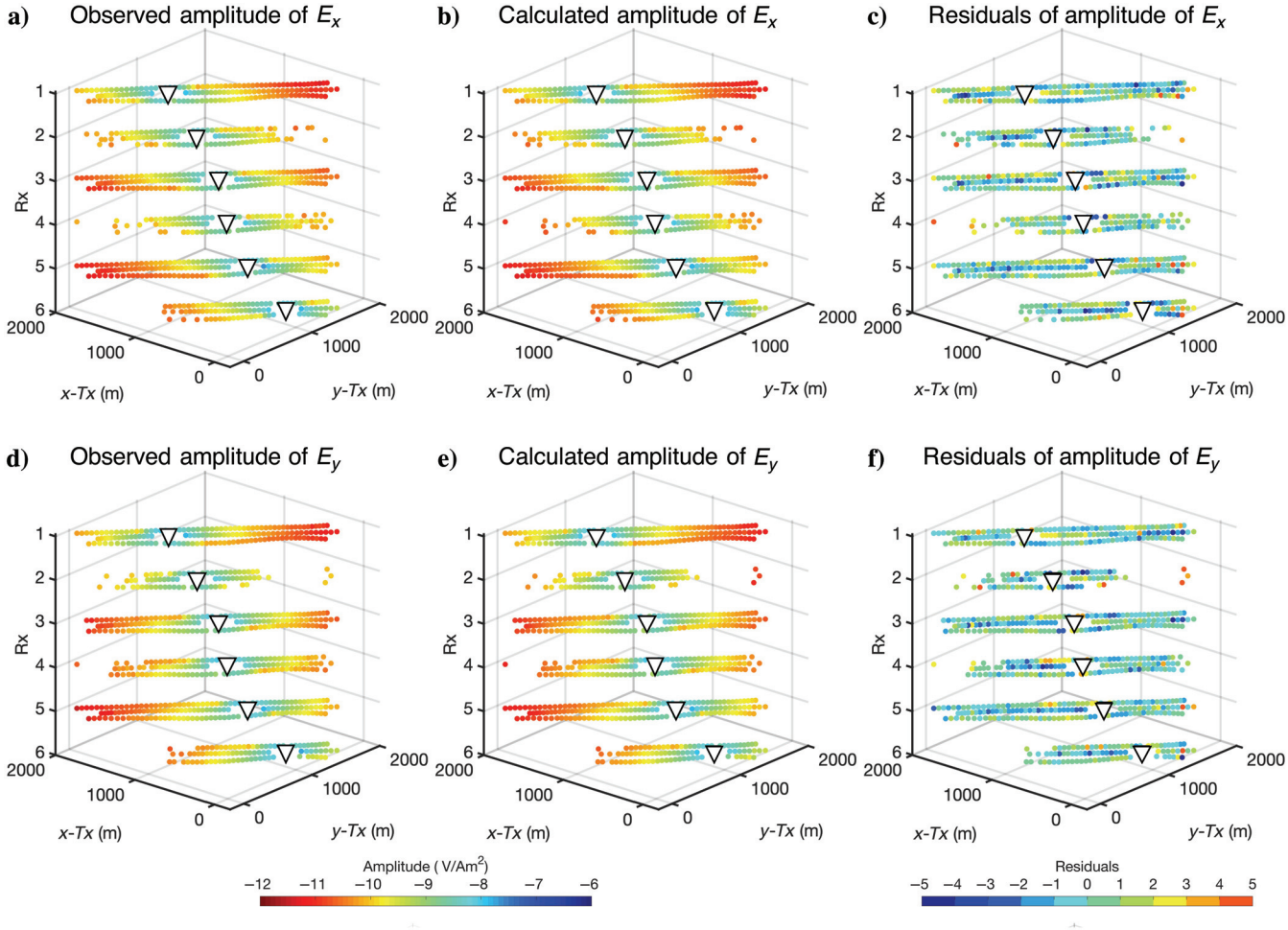

Figure 10. Electric field data measured using OBE receivers at a frequency of 0.125 Hz in the Ieyama hydrothermal area. The electric field data are normalized by the source dipole moment (2.16 kAm for 0.125 Hz). The triangles represent the receiver positions. The stacked data points are shown on transmitter positions: (a) observed amplitude of E_x $(\mathrm{V/Am^2})$, (b) calculated amplitude of E_x $(\mathrm{V/Am^2})$ from the inverted model shown in Figure 11, (c) residuals of E_x amplitude data, (d) observed amplitude of E_y $(\mathrm{V/Am^2})$, (e) calculated amplitude of E_y $(\mathrm{V/Am^2})$ from the inverted model shown in Figure 11, and (f) residuals of E_y amplitude data. Data residuals, defined as the difference between the observed and calculated data for the inverted model, are standardized by dividing by their corresponding error. The stacking window is 68 s, corresponding to a sample interval of approximately 45 m with the horizontal movement of the transmitter.

shape generally follows topography; topography was obtained using a shipboard multibeam echosounder system (Kasaya et al., 2020). It was worth mentioning that the finite-element method with unstructured tetrahedral meshes is an attractive option for accurate modeling of seafloor topography (Schwarzbach et al., 2011; Wang et al., 2018). We incorporated the position, direction, and dipping of the source dipole measured by the SSBL and the altimeter into the inversion.

We initially set the target rms misfit to 1.0, whereas the rms misfit for the starting model was 5.6, and this misfit was reduced to 1.5 following 10 iterations. Although the rms misfit could reach 1.4 (by continuing the inversion iteration), the inverted model with an rms misfit of 1.4 showed patchy structures; as such, an rms misfit of 1.5 was selected as the most suitable. To obtain the minimum norm model with a new target rms misfit of 1.5, we conducted an additional Occam Phase II with the target rms misfit; Figure 11 displays the model obtained from Occam Phase II. The calculated CSEM responses from the resistivity model fit the observed data (Figure 10).

The obtained model (Figure 11) reveals subseafloor conductive zones immediately below the seafloor (C1, C2, and C3). The resistivity values (0.1–0.3 ohm-m) are lower than the seawater resistivity (0.3 ohm-m). The C1 $\{(x, y)$: 1000 m $< x <$ 1400 m, 200 m $< y <$ 500 m, and 1040 m $< z <$ 1080 m$\}$ and C3 $\{(x, y)$: 0 m $< x <$ 500 m, 800 m $< y <$ 1400 m, and 1050 m $< z <$ 1120 m$\}$ are imaged northwest and southeast of the depression center. Hydrothermal activity on the seafloor is not observed at C1 and C3. The C2 $\{(x, y)$: 600 m $< x <$ 1000 m, 300 m $< y <$ 500 m, and 1060 m $< z <$ 1080 m$\}$ is imaged below the mound structures and the negative SP area. We use the seawater resistivity (0.3 ohm-m) as a threshold for the size estimate of C1–C3. A vertical conductive zone C4 $\{(x, y)$: 700 m $< x <$ 900 m, 500 m $< y <$ 700 m, and 1080 m $< z <$ 1200 m$\}$ is imaged below the hydrothermal plume area. The resistivity values of C4 are approximately 0.3 ohm-m. The C4 extends from the seafloor to a deeper conductive zone of C5 $\{(x, y)$: 800 m $< x <$ 1300 m, 400 m $< y <$ 800 m, and 1200 m $< z <$ 1500 m$\}$. The resistivity values of C5 are approximately 0.4 ohm-m. We calculate the conductance as the integrated conductivity-thickness product over the top 50 m below the seafloor in the model, and the high conductance is observed at C1–C4 (Figure 11b and 11c).

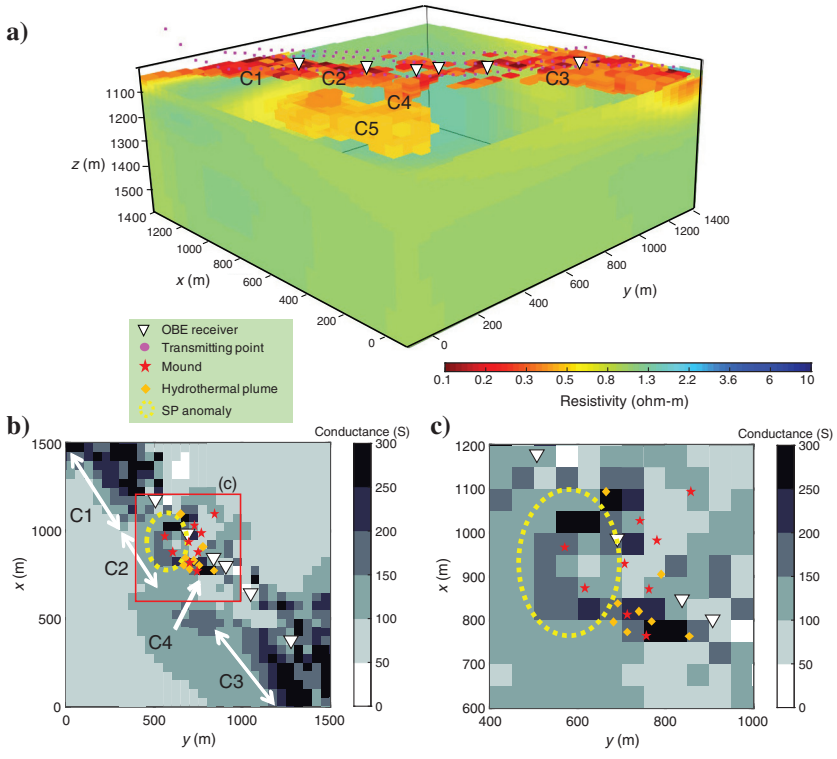

Figure 11. Resistivity model from the 3D inversion of the observed data overlain with the positions of transmitters (the magenta circles) and receivers (triangles). Designations C1, C2, and C3 denote subseafloor electric conductive zones immediately below the seafloor; C4 denotes a vertical conductive zone extending from the seafloor to a deeper conductive zone of C5. (b) Map view of conductance over the top 50 m below the seafloor with the positions of mounds (the red stars), hydrothermal plumes (the orange rhombus), and SP anomaly area (the dashed yellow lines). (c) Magnified view of the active hydrothermal zone outlined by the red box in (b). Note that the color of the mound is changed from Figure 9b to improve visibility.

Sensitivity test

A sensitivity test was conducted to evaluate the ability of the CSEM data to constrain conductive anomalies below the seafloor. The sensitivity test model consisted of a 1.0 ohm-m background and a 0.1 ohm-m conductive anomaly with different spatial extensions embedded in the background at two seafloor locations (Figure 12a); the models included fixed parameters for seawater (0.304 ohm-m). A synthetic CSEM data set was generated from the model using forward modeling. The survey configuration of the synthetic data set (i.e., transmitter-receiver pairs, frequencies, and measured EM components) was identical to our field data. Therefore, the synthetic data set consisted of 3833 independent amplitude data of E_x and E_y with different transmitter-receiver pairs and frequencies. Then, Gaussian random noise (5–50% corresponding to individual error bars of the actual field data) was included to carry out a realistic test, and an error bar similar to the field data was used for all data. The starting and prior models for the inversion were a 1.0 ohm-m homogeneous half-space. The models included the topography of the Ieyama hydrothermal area.

The inversion of the synthetic data set recovered the minimum norm model with a target rms misfit of 1.0 after five iterations (Figure 12b). The resistivity values and shapes of the imaged anomalies resembled those of the true models. The conductive anomalies were well recovered on all y-sections, indicating that data quality was not spatially biased. Based on this inversion result, we concluded that the observed CSEM data are able to constrain the conductive anomalies of the SMS.

Data measurement error

The observation error of the CSEM data largely originates from the geometric measurement errors of the transmitters and receivers; as such, the geometric measurement error can affect the inversion results (Weitemeyer and Constable, 2014; Gehrmann et al., 2020). The SSBL

DOI:10.1190/geo2021-0328.1

system recorded the positions of four self-popup OBE receivers immediately after the deployment, not during transmitter tows. The SSBL measured the position of the target object every 10 s during the SSBL measurement, and the position error of each SSBL measurement was approximately 10 m. SSBL measurements were conducted for 20 min for each self-popup receiver. The SSBL measurements for 20 min decreased uncertainty by less than 1 m for the positions of four self-popup OBE receivers. The positioning error of two mobile OBE receivers deployed by ROV was estimated to be less than 5 m using a Doppler velocity log navigation for ROV.

The SSBL system recorded the positions of the MEMSYS transmitter during tows. Seven SSBL measurements more than 68 s (32 s: completing four cycles of 0.125 Hz square waves and 36 s: transmitter off) estimated the transmitter position of each stacked data. The estimated uncertainty was less than 4 m for the transmitter position of each stacked data; as a result, the processed CSEM data contained errors of up to 5 m in transmitter-receiver offset for the four self-popup OBE receivers (i.e., 1 m error of the receivers + 4 m error of the transmitter). The minimum offset of the CSEM data used for the inversion was 150 m, and the maximum offset was 2 km. The offset errors were estimated to be 3.3% and 0.25% for the minimum offset of 150 m and the maximum offset of 2 km for the four self-popup OBE receivers. The processed CSEM data contained errors of up to 9 m in transmitter-receiver offset for the two mobile OBE receivers (i.e., 5 m error of the receivers + 4 m error of the transmitter). For the two mobile OBE receivers, the offset error for the minimum offset of 150 m was estimated to be 6%, and the offset error for a maximum offset of 1.5 km was estimated to be 0.45%. This estimation demonstrated that the geometric error of the transmitter and receiver is sufficiently small for the CSEM survey.

We estimated the observation error of our CSEM data in a stacking window containing four cycles of the transmitted waveform. In general, observation errors are estimated in a stacking window containing a few tens of transmitted waveforms (Myer et al., 2011). To ascertain whether the estimation in the survey data was valid to apply to imaging SMS, we compared inverted models resulting from the stacked data of four wave cycles (each stacking window of 68 s) and six wave cycles (each stacking window of 108 s). The stacking windows of 68 s and 108 s corresponded to a sample interval of approximately 45 m and 72 m with the horizontal movement of the transmitter, respectively. The procedure for estimating the error bars for this six-cycle data was the same as that used for the four-cycle data.

The resulting inverted resistivity model of the six-cycle stacking data set was almost equivalent to that of the four-cycle stacking data set, with the exception of some portions (Figure 13a and 13b). Figure 13c shows the normalized difference between the two models. The differences were attributed to the ambiguities in the estimation of observation error. Although four- or six-cycle stacking was insufficient to estimate the standard error of observed data statistically, the similarity between the two models indicated that a practically reasonable standard error was obtained using four wave cycles. However, C1 suffered from high ambiguities due to the observation error estimation (Figure 13). The result of the four-cycle stacking data set suggested that SMS deposits are extended at the surface near C1, compared with the results of the six-cycle stacking data set. This indicated that we need to be careful about interpreting the extent of the SMS deposits. We will collect seafloor sampling of the SMS deposits around C1 to determine the

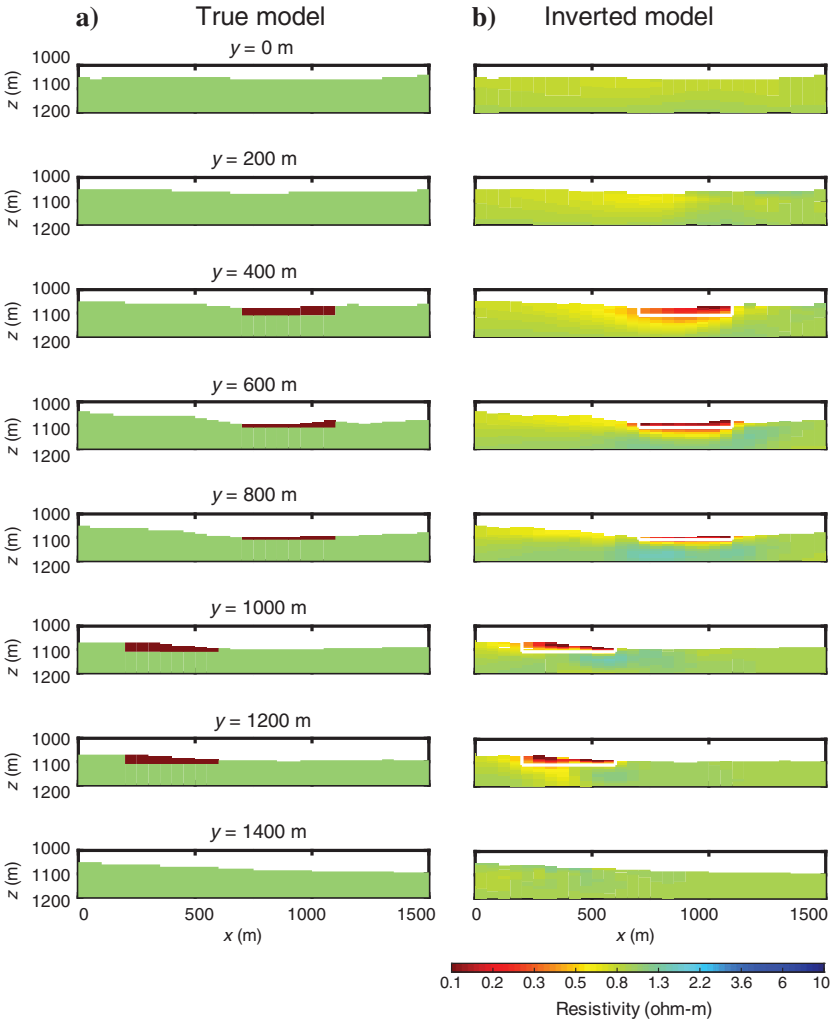

Figure 12. (a) Synthetic resistivity model based on an actual field survey from the Ieyama hydrothermal area used to evaluate the ability of the CSEM data to constrain conductive anomalies below the seafloor. This model consists of a 1.0 ohm-m background and a 0.1 ohm-m conductive anomaly with different spatial extensions embedded in the background at two seafloor locations. Synthetic CSEM data have been generated from the model using forward modeling, with 3833 data numbers from the same survey configuration as the field data. We have added Gaussian random noise (5–50% corresponding to individual error bars of the actual data) to the synthetic data set to carry out a realistic test, and error bars similar to the actual data have been used for all data. (b) Inverted resistivity model from synthetic data. The white lines mark the outline of the true conductive anomalies.

extent to which the SMS deposits extend horizontally. There also was a large error regarding the geometry of C5. Therefore, when interpreting C5, we need to be careful about the ambiguity of its spread.

Detection and verification of potential SMS zones

We identify potential SMS zones based on the resistivity model shown in Figure 11. The resistivity values of the shallow conductive zones (C1–C3) are 0.1–0.3 ohm-m, interpreted as the potential SMS zones below the seafloor. The resistivity values of C1, C2, and C3 (which are lower than the seawater resistivity value) are consistent with the resistivity values of SMS measured in other hydrothermal areas (Haroon et al., 2018; Müller et al., 2018; Gehrmann et al., 2019; Ishizu et al., 2019). Only rocks with large porosity (>25%) and high-temperature pore fluids (>300°C) are able to explain the median 0.2 ohm-m (i.e., resistivity values 0.1–0.3 ohm-m of C1–C3) if no SMS is included there (Ishizu et al., 2019). Hydrothermal activity on the seafloor is low at C1 and C3, based on the acoustic mapping of the hydrothermal plume and ROV camera observations (Kasaya et al., 2020). Although C2 contains an active hydrothermal zone above the vertical conductive zone (C4), much of C2 is not hydrothermally active. This implies that these low-resistivity features result from SMS rather than conductive hydrothermal fluids. Rocks with 0.2 ohm-m bulk resistivity in the Iheya hydrothermal field include 5% fine-grained sulfide minerals, such as pyrite, galena, and chalcopyrite (Ishizu et al., 2019). The negative SP anomaly and mounds at C2 indicate that this zone is related to SMS deposits near the seafloor. Conversely, hydrothermal plumes, mounds, and SP anomalies are not detected in C1 and C3. The areas around C1 and C3 are covered by mud (Kasaya et al., 2020); therefore, C1 and C3 are likely unrelated to recent hydrothermal activities. They may be old SMS deposits buried below the seafloor by sedimentation after they formed.

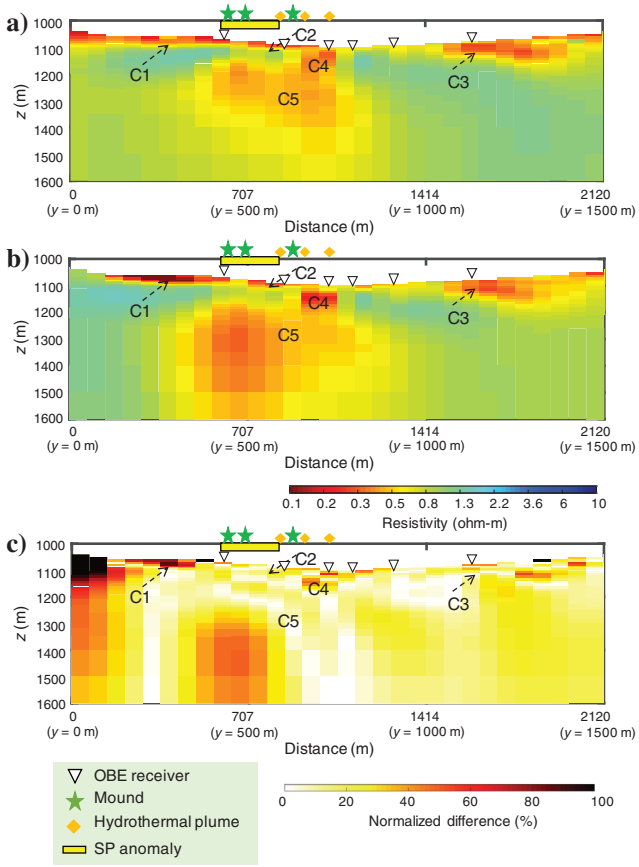

Figure 13. The 2D sections along line 1 (the dashed white line in Figure 9b) of (a) m_{ref}: an inverted resistivity model from the data set with each stacking window of 68 s (32 s: four cycles of 8 s square waves and 36 s: three times of 12 s transmitter off) and (b) m_{per}: an inverted resistivity model from the data set with each stacking window of 108 s (48 s: six cycles of 8 s square waves and 60 s: five times of 12 s transmitter off). The m_{ref} is the same as the model shown in Figure 11. (c) Uncertainty of the inverted model attributable to the estimates of the observation error. The uncertainty is defined as the normalized difference: $|m_{per} - m_{ref}/m_{ref}| \times 100\%$. The stacking windows of 68 s and 108 s correspond to a sample interval of approximately 45 m and 72 m with the horizontal movement of the transmitter, respectively.

The vertical conductive zone (C4) with a resistivity value of 0.3 ohm-m is imaged below the hydrothermal plumes (Figure 11). The hydrothermal activity is relatively high on the seafloor at C4 (Kasaya et al., 2020). The positional correspondence between C4 and the seafloor hydrothermal plumes indicates that C4 is a potential conduit of hydrothermal fluid, upwelling from the deep subseafloor. The upwelling fluids are discharged to the seafloor, and discharged fluids are likely detected as hydrothermal plumes. A deeper conductive zone of C5 is connected to C4 and probably acts as a hydrothermal reservoir from which fluids flow to C4. Although C4 and C5 may include SMS, the higher resistivity of C4 and C5 than C1–C3 implies that C4 and C5 are primarily attributed to conductive fluids as opposed to SMS.

Each conductor (i.e., C1–C3) has a horizontal size of several hundred meters (200–500 m) and a thickness of several tens of meters (25–50 m). Assuming that these conductors consist of SMS, each SMS size is comparable to that of another SMS zone confirmed by drilling data in the Izena hydrothermal area (de Sá et al., 2020) and the TAG mound (Murton et al., 2019). Although no drilling has been carried out in this survey area, the geometrical consistency with previous studies on SMS demonstrates that this CSEM survey with 3D inversion can delineate the typical SMS distribution. Based on the 3D resistivity structures, we suggest that C1–C3 are potential SMS zones in the Ieyama hydrothermal area.

CONCLUSION

The cost of a 3D CSEM survey largely depends on the number of deployed OBE receivers. This study proposes a cost-effective 3D marine CSEM survey using fewer OBE receivers than the survey with a receiver deployment in a grid pattern to reduce survey costs for SMS. The proposed CSEM survey uses a line of OBE receivers in the center of the survey area and several transmitter towlines. By contrast, the 3D survey with a receiver deployment in a grid pattern uses several lines of OBE receivers with several transmitter towlines. Numerical tests demonstrate that the proposed survey (seven OBE receivers) using 80% fewer receivers than a survey with a receiver deployment in a grid pattern (35 OBE receivers) accurately delineates resistors and conductors distributed at different seafloor locations, obtaining a performance similar to that of the conventional survey. This demonstrates a high cost-effectiveness of the proposed survey. The proposed survey also is advantageous in terms of reducing the computation time; this is reduced by 34% compared to the conventional survey for a synthetic example. The synthetic

test demonstrates that the proposed survey using fewer OBE receivers also is effective in mapping a realistic SMS model.

We have explored SMS in the Ieyama hydrothermal area off Okinawa, southwest Japan, using the proposed 3D CSEM survey; this survey uses a line of six OBE receivers in the survey center and three transmitter towlines. The resulting 3D resistivity distribution from the observed data highlights three potential SMS zones consisting of 0.2 ohm-m low resistivity embedded into 1 ohm-m sediment. The size of each potential SMS zone is comparable to that of another SMS zone in the TAG mound. The resistivity distribution also specifies a vertical conductor representing a potential conduit for hydrothermal fluids.

ACKNOWLEDGMENTS

We would like to thank three anonymous reviewers, R. Mittet, J. Blanch, and J. Etgen, for their detailed and valuable comments that led to significant improvements in this paper. We thank the captain, crew, and technicians of the KM 17-10 cruise survey for assisting the field operation, G. Li and Y. Li for providing CSEM responses in Figure A-2, and Y. Ogawa for allowing us to use his computer system. This work was supported by the Kyoto University Foundation, the Japan Society for the Promotion of Science KAKENHI (grant nos. 26289347, 18H03894, 18H03733, and 17J08764), and the Cross-ministerial Strategic Innovation Promotion Program "Next Generation Technology for Ocean Resources Exploration." Figure 9 was produced using Generic Mapping Tools software (https://www.soest.hawaii.edu/gmt).

DATA AND MATERIALS AVAILABILITY

Data associated with this research are confidential and cannot be released.

APPENDIX A

3D CSEM FORWARD MODELING AND ITS VALIDATION

The 3D CSEM forward modeling uses the FDM method combined with a scattered field approach. The scattered field approach splits electric fields into a primary and secondary field to exclude source-point singularities from the numerical computations (Newman and Alumbaugh, 1997; Weiss and Constable, 2006; Streich, 2009; da Silva et al., 2012; Li et al., 2018). Using the scattered field approach, we solve the vector Helmholtz equation for the secondary electric field:

$$-\nabla \times \nabla \times \mathbf{E}^{\mathrm{s}} + i\omega\mu\sigma\mathbf{E}^{\mathrm{s}} + i\omega\mu(\sigma - \sigma^{\mathrm{p}})\mathbf{E}^{\mathrm{p}} = 0, \quad \text{(A-1)}$$

where ω denotes the angular frequency of the field assuming time-dependence of the form $e^{-i\omega t}$, μ expresses the magnetic permeability, σ signifies the conductivity, σ^{p} represents the background layered earth conductivity for the primary field computation, $\mathbf{E}^{\mathrm{p}}$ represents the primary electric field, and $\mathbf{E}^{\mathrm{s}}$ denotes the secondary electric field.

Primary electric fields are analytically calculated by solving the Hankel transform in a layered background model (Key, 2009; Li and Li, 2016). The layered background model for computing primary fields consists of air, sea, and seafloor homogeneous half-space. The primary fields are time-consuming to compute because they must be computed for all FDM grids per transmitter and frequency. To shorten the computation time of primary fields, we apply parallel implementation with MPI processes. The computation is parallelized over grids. All primary fields are computed only once at the beginning of our code. The computed primary fields are stored and reused for each forward calculation.

We apply FDM with a staggered grid to equation A-1, resulting in a linear system:

$$\mathbf{A}\mathbf{E}^{\mathrm{s}} = \mathbf{b}, \quad \text{(A-2)}$$

where $\mathbf{A}$ is complex, sparse, and symmetric positive definite and $\mathbf{b}$ is a vector, including the primary field information and the Dirichlet boundary condition of the secondary electric field. A multicore parallel sparse direct solver PARDISO (Schenk, 2022) via Intel Math Kernel Library (MKL) is used to solve the linear system (Schenk and Gärtner, 2004). The direct forward solvers are suitable for multisource marine CSEM modeling because the expensive matrix factorization needs to be performed only once, and then multiple forward solutions can be computed cheaply (Börner et al., 2008; Streich, 2009; Grayver et al., 2013; Key, 2016; Puzyrev et al., 2016; Cai et al., 2017; Castillo-Reyes et al., 2019). The computed secondary field is added to the primary field to obtain the total electric field.

The forward modeling algorithm is validated using a 3D example of an oil field model (Figure A-1). The model consists of an air layer with 10^8 ohm-m resistivity, a seawater layer with 0.3 ohm-m resistivity and 1 km thickness, and a reservoir with 100 ohm-m resistivity embedded in a seafloor layer with 1 ohm-m resistivity. The reservoir is a cuboid with 4 km length, 4 km width, and 100 m height at 1 km depth below the seafloor. The center of the reservoir corresponds to $x = 5$ km and $y = 5$ km. A transmitter using an HED oriented along the y-direction is at $x = 5$ km and $y = 5$ km at a height 100 m above the seafloor. In addition, 50 receivers are deployed on the seafloor at 200 m intervals from $y =$ 0 to 10 km at $x = 5$ km (except $y = 5$ km). The forward modeling calculation is performed on a grid of $98 \times 98 \times 65$ cells, including several boundary cells. For the horizontal cells, a 200 m grid is used in the interest region $\{(x, y)$: 0 km $< x, y <$ 10 km$\}$. A 100 m grid is used in the region close to the transmitter $\{(x, y)$: 2 km $< x,$ $y <$ 8 km$\}$. We append several boundary cells at each side, growing in size at a stretching factor of 2.0. For the vertical grid, fine grids are used close to the transmitters. The grid size increases gradually with increasing distance from the transmitters. The primary field is calculated from the layered earth consisting of the air, sea, and seafloor. The primary model is equivalent to a model deleting the reservoir from Figure A-1. The anomaly structure for generating secondary fields is the oil reservoir.

For evaluation of the solutions, the relative error for the amplitude of CSEM response and the absolute error for the phase of CSEM response are defined as

$$\text{Relative error}(\%) = 100\times\left|\frac{R_{\mathrm{cal}} - R_{\mathrm{ref}}}{R_{\mathrm{ref}}}\right| \quad \text{(A-3)}$$

and

$$\text{Absolute error} = |R_{\mathrm{cal}} - R_{\mathrm{ref}}|, \quad \text{(A-4)}$$

where R_{cal} and R_{ref}, respectively, denote the calculated response by our forward modeling algorithm and the reference response from Li et al. (2018).

Figure A-2 presents our solutions compared with 3D solutions obtained using the forward modeling algorithm of Li et al. (2018) at a frequency of 0.25 Hz. The discrepancy between our responses and solutions obtained by Li et al. (2018) is less than 2.2% in amplitude for E_y, E_z, and H_x. The absolute error of the phase is less than 1.8° for E_y, E_z, and H_x. We conclude that our forward modeling can produce sufficiently accurate responses for this case. However, the reader is reminded that the solutions by Li et al. (2018) cannot be treated as exact as for analytical 1D solutions. Nevertheless, they are useful as reference solutions. The discrepancy might result from the difference in boundary conditions (Dirichlet versus perfectly matched layer), the staggering scheme (electric field components versus magnetic field components are on the edges), mesh design, or all of the above.

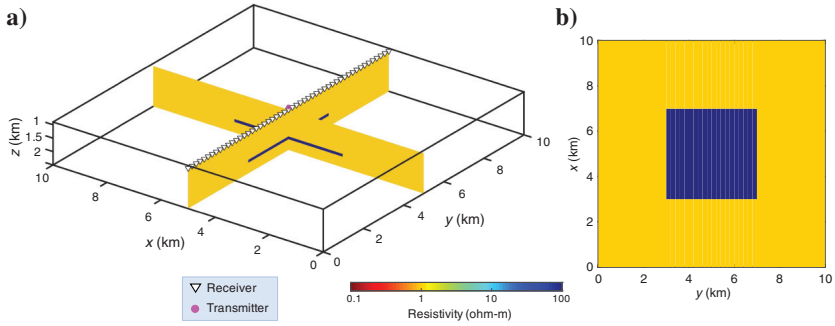

Figure A-1. A 3D model for validating our forward modeling algorithm. (a) A 3D canonical oil reservoir model shown in Figure 7 of Li et al. (2018). The model includes two layers of air and seawater and a 3D oil reservoir in the ranges of 3 km < x and y < 7 km and 2 km < z < 2.1 km, embedded in a seafloor half-space. A magenta circle denotes the transmitter position; the white triangles denote the receiver positions. Here, z shows depth from the sea surface. (b) Horizontal slice of the model at $z = 2$ km.

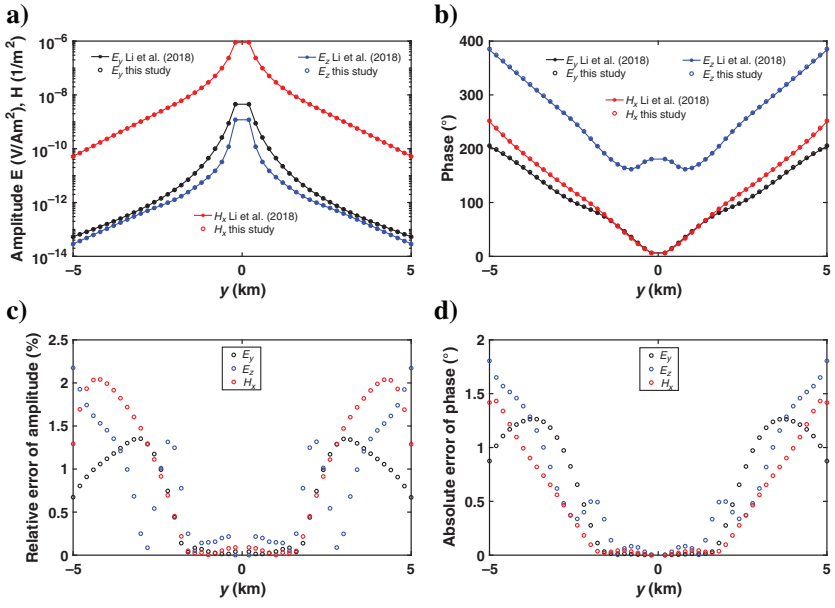

Figure A-2. Numerical solutions at a frequency of 0.25 Hz for the 3D model shown in Figure A-1. (a) Amplitude of the electric field $\mathbf{E}$ (V/Am^2) and magnetic field $\mathbf{H}$ (1/m^2) and (b) phase of $\mathbf{E}$ and $\mathbf{H}$ (°). The open circle denotes responses from our forward modeling algorithm. The solid lines show responses from Li et al. (2018). The black, blue, and red symbols denote E_y, E_z, and H_x, respectively. (c) Relative error of amplitude for $\mathbf{E}$ and $\mathbf{H}$ between solutions from our code and responses from Li et al. (2018). (d) Absolute error of phase.

APPENDIX B

DETAIL OF MODEL UPDATE IN THE OCCAM INVERSION ALGORITHM

Before the solution of equation 7, matrix $\mathbf{C}_m\mathbf{J}_k^T$ is first computed by inverting $\mathbf{C}_m^{-1}$ using PARDISO (Schenk and Gärtner, 2004). The regularization $\mathbf{C}_m^{-1}$ is nonnegative definite and singular. To make it positive definite, a small value of 10^{-4} is added to its diagonal before inversion (Kordy et al., 2016). Then, matrix multiplication $\mathbf{J}_k$ and $\mathbf{C}_m\mathbf{J}_k^T$ for $\mathbf{J}_k\mathbf{C}_m\mathbf{J}_k^T$ is implemented using dgemm from Intel MKL (Intel, 2022). The dgemm routine calculates the product of double-precision matrices. We solve the dense and symmetric $N \times N$ matrix using a parallel direct solver of dposv from Intel MKL using the Cholesky decomposition (Intel, 2022). Solvers of PARDISO, dgemm, and dposv use parallel computations in the shared memory. Using many threads reduces the computation time.

At every iteration of the Occam algorithm, we search for λ that gives the model with the minimum misfit in phase I or at the desired misfit in phase II (Constable et al., 1987; Siripunvaraporn and Egbert, 2000; Key, 2009). In phase I, the Nelder-Mead search method (Nelder and Mead, 1965) through $\log_{10}\lambda$ is used to find λ with the minimum misfit. In phase II, Brent's method is used to find the largest λ providing the desired level of the misfit. Brent's method is a hybrid root-finding algorithm combining the bisection method, the secant method, and inverse quadratic interpolation (Press et al., 1992). If the minimum search fails to find a model with a lower misfit, then a reduced step of updating the model is taken using model $\mathbf{m}'_{k+1}$ (Key, 2009), as shown here:

$$\mathbf{m}'_{k+1} = \alpha\mathbf{m}_{k+1} + (1-\alpha)\mathbf{m}_k. \qquad \text{(B-1)}$$

Initially, step size α is set as one. Then, α is successively cut in half until a better-fitting model is obtained (Key, 2009).

REFERENCES

Abubakar, A., T. M. Habashy, M. Li, and J. Liu, 2009, Inversion algorithms for large-scale geophysical electromagnetic measurements: Inverse Problems, **25**, 123012, doi: 10.1088/0266-5611/25/12/123012.

Attias, E., D. Thomas, D. Sherman, K. Ismail, and S. Constable, 2020, Marine electrical imaging reveals novel freshwater transport mechanism in Hawai'i: Science Advances, **6**, eabd4866, doi: 10.1126/sciadv.abd4866.

Attias, E., K. Weitemeyer, S. Hölz, S. Naif, T. A. Minshull, A. I. Best, A. Haroon, M. Jegen-Kulcsar, and C. Berndt, 2018, High-resolution resistivity imaging of marine gas hydrate structures by combined inversion of CSEM towed and ocean-bottom receiver

data: Geophysical Journal International, **214**, 1701–1714, doi: 10.1093/gji/ggy227.
Attias, E., K. Weitemeyer, T. A. Minshull, A. I. Best, M. Sinha, M. Jegen-Kulcsar, S. Hölz, and C. Berndt, 2016, Controlled-source electromagnetic and seismic delineation of subseafloor fluid flow structures in a gas hydrate province, offshore Norway: Geophysical Journal International, **206**, 1093–1110, doi: 10.1093/gji/ggw188.
Baba, K., N. Tada, H. Utada, and W. Siripunvaraporn, 2013, Practical incorporation of local and regional topography in three-dimensional inversion of deep ocean magnetotelluric data: Geophysical Journal International, **194**, 348–361, doi: 10.1093/gji/ggt115.
Blatter, D., K. Key, A. Ray, C. Gustafson, and R. Evans, 2019, Bayesian joint inversion of controlled source electromagnetic and magnetotelluric data to image freshwater aquifer offshore New Jersey: Geophysical Journal International, **218**, 1822–1837, doi: 10.1093/gji/ggz253.
Börner, R.-U., O. G. Ernst, and K. Spitzer, 2008, Fast 3-D simulation of transient electromagnetic fields by model reduction in the frequency domain using Krylov subspace projection: Geophysical Journal International, **173**, 766–780, doi: 10.1111/j.1365-246X.2008.03750.x.
Boschen, R. E., A. A. Rowden, M. R. Clark, and J. P. Gardner, 2013, Mining of deep-sea seafloor massive sulfides: A review of the deposits, their benthic communities, impacts from mining, regulatory frameworks and management strategies: Ocean & Coastal Management, **84**, 54–67, doi: 10.1016/j.ocecoaman.2013.07.005.
Cai, H., X. Hu, J. Li, M. Endo, and B. Xiong, 2017, Parallelized 3D CSEM modeling using edge-based finite element with total field formulation and unstructured mesh: Computers & Geosciences, **99**, 125–134, doi: 10.1016/j.cageo.2016.11.009.
Cairns, G. W., R. L. Evans, and R. N. Edwards, 1996, A time domain electromagnetic survey of the TAG hydrothermal mound: Geophysical Research Letters, **23**, 3455–3458, doi: 10.1029/96GL03233.
Castillo-Reyes, O., J. de la Puente, L. E. García-Castillo, and J. M. Cela, 2019, Parallel 3-D marine controlled-source electromagnetic modelling using high-order tetrahedral Nédélec elements: Geophysical Journal International, **219**, 39–65, doi: 10.1093/gji/ggz285.
Chave, A. D., 2009, On the electromagnetic fields produced by marine frequency domain controlled sources: Geophysical Journal International, **179**, 1429–1457, doi: 10.1111/j.1365-246X.2009.04367.x.
Chave, A. D., and C. S. Cox, 1982, Controlled electromagnetic sources for measuring electrical conductivity beneath the oceans: 1. Forward problem and model study: Journal of Geophysical Research, Solid Earth, **87**, 5327–5338, doi: 10.1029/JB087iB07p05327.
Commer, M., and G. A. Newman, 2008, New advances in three-dimensional controlled-source electromagnetic inversion: Geophysical Journal International, **172**, 513–535, doi: 10.1111/j.1365-246X.2007.03663.x.
Constable, S., 2010, Ten years of marine CSEM for hydrocarbon exploration: Geophysics, **75**, no. 5, 75A67–75A81, doi: 10.1190/1.3483451.
Constable, S., 2013, Review paper: Instrumentation for marine magnetotelluric and controlled source electromagnetic sounding: Geophysical Prospecting, **61**, 505–532, doi: 10.1111/j.1365-2478.2012.01117.x.
Constable, S., P. K. Kannberg, and K. Weitemeyer, 2016, Vulcan: A deep-towed CSEM receiver: Geochemistry, Geophysics, Geosystems, **17**, 1042–1064, doi: 10.1002/2015GC006174.
Constable, S., P. Kowalczyk, and S. Bloomer, 2018, Measuring marine self-potential using an autonomous underwater vehicle: Geophysical Journal International, **215**, 49–60, doi: 10.1093/gji/ggy263.
Constable, S. C., R. L. Parker, and C. G. Constable, 1987, Occam's inversion: A practical algorithm for generating smooth models from electromagnetic sounding data: Geophysics, **52**, 289–300, doi: 10.1190/1.1442303.
Cox, C. S., S. C. Constable, A. D. Chave, and S. C. Webb, 1986, Controlled-source electromagnetic sounding of the oceanic lithosphere: Nature, **320**, 52–54, doi: 10.1038/320052a0.
da Silva, N. V., J. V. Morgan, L. MacGregor, and M. Warner, 2012, A finite element multifrontal method for 3D CSEM modeling in the frequency domain: Geophysics, **77**, no. 2, E101–E115, doi: 10.1190/geo2010-0398.1.
de Sá, V. R., K. Koike, T. Goto, T. Nozaki, Y. Takaya, and T. Yamasaki, 2020, A combination of geostatistical methods and principal components analysis for detection of mineralized zones in seafloor hydrothermal systems: Natural Resources Research, **30**, 2875–2887, doi: 10.1007/s11053-020-09705-4.
deGroot-Hedlin, C., and S. Constable, 1990, Occam's inversion to generate smooth, two-dimensional models from magnetotelluric data: Geophysics, **55**, 1613–1624, doi: 10.1190/1.1442813.
Dehiya, R., A. Singh, P. K. Gupta, and M. Israil, 2017, 3-D CSEM data inversion algorithm based on simultaneously active multiple transmitters concept: Geophysical Journal International, **209**, 1004–1017, doi: 10.1093/gji/ggx062.
Du, Z., and K. Key, 2018, Case study: North Sea heavy oil reservoir characterization from integrated analysis of towed-streamer EM and dual-sensor seismic data: The Leading Edge, **37**, 608–615, doi: 10.1190/tle37080608.1.
Dunham, M. W., S. Ansari, and C. G. Farquharson, 2018, Application of 3D marine controlled-source electromagnetic finite-element forward modeling to hydrocarbon exploration in the Flemish Pass Basin offshore Newfoundland, Canada: Geophysics, **83**, no. 2, WB33–WB49, doi: 10.1190/geo2017-0451.1.
Egbert, G. D., and A. Kelbert, 2012, Computational recipes for electromagnetic inverse problems: Geophysical Journal International, **189**, 251–267, doi: 10.1111/j.1365-246X.2011.05347.x.
Eidesmo, T., S. Ellingsrud, L. M. MacGregor, S. Constable, M. C. Sinha, S. Johansen, F. N. Kong, and H. Westerdahl, 2002, Sea bed logging (SBL), a new method for remote and direct identification of hydrocarbon filled layers in deepwater areas: First Break, **20**, 144–152, doi: 10.1046/j.1365-2397.2002.00264.x.
Engelmark, F., J. Mattsson, A. McKay, and Z. Du, 2014, Towed streamer EM comes of age: First Break, **32**, 75–78, doi: 10.3997/1365-2397.32.4.74381.
Evans, R. L., 2007, Using CSEM techniques to map the shallow section of seafloor: From the coastline to the edges of the continental slope: Geophysics, **72**, no. 2, WA105–WA116, doi: 10.1190/1.2434798.
Evans, R. L., M. C. Sinha, S. C. Constable, and M. J. Unsworth, 1994, On the electrical nature of the axial melt zone at 13°N on the East Pacific Rise: Journal of Geophysical Research, **99**, 577–588, doi: 10.1029/93JB02577.
Everett, M. E., and A. D. Chave, 2019, On the physical principles underlying electromagnetic induction: Geophysics, **84**, no. 5, W21–W32, doi: 10.1190/geo2018-0232.1.
Expedition 331 Scientists, 2010, Deep hot biosphere: IODP Preliminary Report, 331.
Gehrmann, R. A. S., A. Haroon, M. Morton, A. T. Djanni, and T. A. Minshull, 2020, Seafloor massive sulphide exploration using deep-towed controlled source electromagnetics: Navigational uncertainties: Geophysical Journal International, **220**, 1215–1227, doi: 10.1093/gji/ggz513.
Gehrmann, R. A. S., L. J. North, S. Graber, F. Szitkar, S. Petersen, T. A. Minshull, and B. J. Murton, 2019, Marine mineral exploration with controlled source electromagnetics at the TAG hydrothermal field, 26°N Mid-Atlantic Ridge: Geophysical Research Letters, **46**, 5808–5816, doi: 10.1029/2019GL082928.
Grayver, A. V., R. Streich, and O. Ritter, 2013, Three-dimensional parallel distributed inversion of CSEM data using a direct forward solver: Geophysical Journal International, **193**, 1432–1446, doi: 10.1093/gji/ggt055.
Gustafson, C., K. Key, and R. L. Evans, 2019, Aquifer systems extending far offshore on the U.S. Atlantic margin: Scientific Reports, **9**, 1–10.
Hannington, M., J. Jamieson, T. Monecke, S. Petersen, and S. Beaulieu, 2011, The abundance of seafloor massive sulfide deposits: Geology, **39**, 1155–1158, doi: 10.1130/G32468.1.
Haroon, A., S. Hölz, R. A. S. Gehrmann, E. Attias, M. Jegen, T. A. Minshull, and B. J. Murton, 2018, Marine dipole-dipole controlled source electromagnetic and coincident-loop transient electromagnetic experiments to detect seafloor massive sulphides: Effects of three-dimensional bathymetry: Geophysical Journal International, **215**, 2156–2171, doi: 10.1093/gji/ggy398.
Herzig, P. M., and M. D. Hannington, 1995, Polymetallic massive sulfides at the modern seafloor a review: Ore Geology Reviews, **10**, 95–115, doi: 10.1016/0169-1368(95)00009-7.
Hesthammer, J., A. Stefatos, M. Boulaenko, A. Vereshagin, P. Gelting, T. Wedberg, and G. Maxwell, 2010, CSEM technology as a value driver for hydrocarbon exploration: Marine and Petroleum Geology, **27**, 1872–1884, doi: 10.1016/j.marpetgeo.2010.08.001.
Hoversten, G. M., R. L. Mackie, and Y. Hua, 2021, Reexamination of controlled-source electromagnetic inversion at the Lona prospect, Orphan Basin Canada: Geophysics, **86**, no. 3, E157–E170, doi: 10.1190/geo2020-0538.1.
Iizasa, K., R. S. Fiske, O. Ishizuka, M. Yuasa, J. Hashimoto, J. Ishibashi, J. Naka, Y. Horii, Y. Fujiwara, A. Imai, and S. Koyama, 1999, A Kurokotype polymetallic sulfide deposit in a submarine silicic caldera: Science, **283**, 975–977, doi: 10.1126/science.283.5404.975.
Intel, 2022, Multiplying Matrices Using dgemm, https://www.intel.com/content/www/us/en/develop/documentation/mkl-tutorial-c/top/multiplying-matrices-using-dgemm.html, accessed 23 April 2022.
Intel, 2022, Developer Reference, https://www.intel.com/content/www/us/en/develop/documentation/onemkl-developer-reference-c/top/lapack-routines/lapack-linear-equation-routines/lapack-linear-equation-driver-routines/posv.html, accessed 23 April 2022.
Ishibashi, J., F. Ikegami, T. Tsuji, and T. Urabe, 2015, Hydrothermal activity in the Okinawa Trough back-arc basin: Geological background and hydrothermal mineralization, *in* J. Ishibashi, K. Okino, and M. Sunamura, eds., Subseafloor biosphere linked to hydrothermal systems: Springer, 337–359.
Ishizu, K., T. Goto, Y. Ohta, T. Kasaya, H. Iwamoto, C. Vachiratienchai, W. Siripunvaraporn, T. Tsuji, H. Kumagai, and K. Koike, 2019, Internal structure of a seafloor massive sulfide deposit by electrical resistivity tomography, Okinawa Trough: Geophysical Research Letters, **46**, 11025–11034, doi: 10.1029/2019GL083749.

Ishizu, K., and Y. Ogawa, 2021, Offshore-onshore resistivity imaging of freshwater using a controlled-source electromagnetic method: A feasibility study: Geophysics, **86**, no. 6, E391–E405, doi: 10.1190/geo2020-0906.1.

Johansen, S. E., M. Panzner, R. Mittet, H. E. Amundsen, A. Lim, E. Vik, M. Landrø, and B. Arntsen, 2019, Deep electrical imaging of the ultraslow-spreading Mohns Ridge: Nature, **567**, 379–383, doi: 10.1038/s41586-019-1010-0.

Kasaya, T., and T. Goto, 2009, A small ocean bottom electromagnetometer and ocean bottom electrometer system with an arm-folding mechanism: Exploration Geophysics, **40**, 41–48, doi: 10.1071/EG08118.

Kasaya, T., T. Goto, H. Iwamoto, and Y. Kawada, 2019, Development of multi-purpose electromagnetic survey instruments: The 13th SEGJ International Symposium, SEGJ, SEG Global Meeting Abstracts, 159–161, doi: 10.1190/SEGJ2018-042.1.

Kasaya, T., J. Kaneko, and H. Iwamoto, 2020, Observation and confirmation based on survey protocol for seafloor massive sulfide deposits using acoustic survey technique and self-potential surveys: BUTSURI-TANSA (Geophysical Exploration), **72**, 155–165.

Kawada, Y., and T. Kasaya, 2017, Marine self-potential survey for exploring seafloor hydrothermal ore deposits: Scientific Reports, **7**, 1–12, doi: 10.1038/s41598-017-13920-0.

Kawada, Y., and T. Kasaya, 2018, Self-potential mapping using an autonomous underwater vehicle for the Sunrise deposit, Izu-Ogasawara arc, southern Japan: Earth, Planets and Space, **70**, 1–15, doi: 10.1186/s40623-018-0913-6.

Key, K., 2009, 1D inversion of multicomponent, multifrequency marine CSEM data: Methodology and synthetic studies for resolving thin resistive layers: Geophysics, **74**, no. 2, F9–F20, doi: 10.1190/1.3058434.

Key, K., 2012, Marine electromagnetic studies of seafloor resources and tectonics: Surveys in Geophysics, **33**, 135–167, doi: 10.1007/s10712-011-9139-x.

Key, K., 2016, MARE2DEM: A 2-D inversion code for controlled-source electromagnetic and magnetotelluric data: Geophysical Journal International, **207**, 571–588, doi: 10.1093/gji/ggw290.

Key, K., S. Constable, T. Matsuno, R. L. Evans, and D. Myer, 2012, Electromagnetic detection of plate hydration due to bending faults at the Middle America Trench: Earth and Planetary Science Letters, **351**, 45–53, doi: 10.1016/j.epsl.2012.07.020.

Komori, S., Y. Masaki, W. Tanikawa, J. Torimoto, Y. Ohta, M. Makio, L. Maeda, J. Ishibashi, T. Nozaki, and O. Tadai, 2017, Depth profiles of resistivity and spectral IP for active modern submarine hydrothermal deposits: A case study from the Iheya North Knoll and the Iheya Minor Ridge in Okinawa Trough, Japan: Earth, Planets and Space, **69**, 1–10, doi: 10.1186/s40623-017-0691-6.

Kordy, M., P. Wannamaker, V. Maris, E. Cherkaev, and G. Hill, 2016, 3-D magnetotelluric inversion including topography using deformed hexahedral edge finite elements and direct solvers parallelized on SMP computers–Part I: Forward problem and parameter Jacobians: Geophysical Journal International, **204**, 74–93, doi: 10.1093/gji/ggv410.

Kowalczyk, P., 2008, Geophysical prelude to first exploitation of submarine massive sulphides: First Break, **26**, 99–106, doi: 10.3997/1365-2397.26.1293.28613.

Letouzey, J., and M. Kimura, 1986, The Okinawa Trough: Genesis of a back-arc basin developing along a continental margin: Tectonophysics, **125**, 209–230, doi: 10.1016/0040-1951(86)90015-6.

Li, G., Y. Li, B. Han, and Z. Liu, 2018, Application of the perfectly matched layer in 3-D marine controlled-source electromagnetic modelling: Geophysical Journal International, **212**, 333–344, doi: 10.1093/gji/ggx382.

Li, Y., and G. Li, 2016, Electromagnetic field expressions in the wavenumber domain from both the horizontal and vertical electric dipoles: Journal of Geophysics and Engineering, **13**, 505–515, doi: 10.1088/1742-2132/13/4/505.

Li, Y., and D. W. Oldenburg, 1996, 3-D inversion of magnetic data: Geophysics, **61**, 394–408, doi: 10.1190/1.1443968.

MacGregor, L. M., S. Constable, and M. C. Sinha, 1998, The RAMESSES experiment—III. Controlled-source electromagnetic sounding of the Reykjanes Ridge at 57°45′N: Geophysical Journal International, **135**, 773–789, doi: 10.1046/j.1365-246X.1998.00705.x.

Meju, M. A., A. S. Saleh, R. L. Mackie, F. Miorelli, R. V. Miller, and N. K. S. Mansor, 2018, Workflow for improvement of 3D anisotropic CSEM resistivity inversion and integration with seismic using cross-gradient constraint to reduce exploration risk in a complex fold-thrust belt in offshore northwest Borneo: Interpretation, **6**, no. 3, SG49–SG57, doi: 10.1190/INT-2017-0233.1.

Micallef, A., M. Person, A. Haroon, B. A. Weymer, M. Jegen, K. Schwalenberg, Z. Faghih, S. Duan, D. Cohen, J. J. Mountjoy, S. Woelz, C. W. Gable, T. Averes, and A. Kumar Tiwari, 2020, 3D characterisation and quantification of an offshore freshened groundwater system in the Canterbury Bight: Nature Communications, **11**, 1–15, doi: 10.1038/s41467-020-14770-7.

Mittet, R., and J. P. Morten, 2012, Detection and imaging sensitivity of the marine CSEM method: Geophysics, **77**, no. 6, E411–E425, doi: 10.1190/geo2012-0016.1.

Morten, J. P., J.-M. Poudroux, and R. Mittet, 2015, Augmenting coarse-grid 3D CSEM with data from a towed-receiver array: 85th Annual International Meeting, SEG, Expanded Abstracts, 889–893, doi: 10.1190/segam2015-5828692.1.

Morten, J. P., J.-M. Poudroux, and R. Mittet, 2016, A modeling study of augmenting coarse-grid 3D controlled-source electromagnetics with data from a towed receiver array: Geophysics, **81**, no. 1, E33–E42, doi: 10.1190/geo2014-0583.1.

Müller, H., K. Schwalenberg, K. Reeck, U. Barckhausen, U. Schwarz-Schampera, C. Hilgenfeldt, and T. von Dobeneck, 2018, Mapping seafloor massive sulfides with the Golden Eye frequency-domain EM profiler: First Break, **36**, 61–67, doi: 10.3997/1365-2397.n0127.

Murton, B. J., B. Lehrmann, A. M. Dutrieux, S. Martins, A. G. de la Iglesia, I. J. Stobbs, F. J. Barriga, J. Bialas, A. Dannowski, and M. E. Vardy, 2019, Geological fate of seafloor massive sulphides at the TAG hydrothermal field (Mid-Atlantic Ridge): Ore Geology Reviews, **107**, 903–925, doi: 10.1016/j.oregeorev.2019.03.005.

Myer, D., S. Constable, and K. Key, 2011, Broad-band waveforms and robust processing for marine CSEM surveys: Geophysical Journal International, **184**, 689–698, doi: 10.1111/j.1365-246X.2010.04887.x.

Myer, D., S. Constable, K. Key, M. E. Glinsky, and G. Liu, 2012, Marine CSEM of the Scarborough gas field, Part 1: Experimental design and data uncertainty: Geophysics, **77**, no. 4, E281–E299, doi: 10.1190/geo2011-0380.1.

Myer, D., K. Key, and S. Constable, 2015, Marine CSEM of the Scarborough gas field, Part 2: 2D inversion: Geophysics, **80**, no. 3, E187–E196, doi: 10.1190/geo2014-0438.1.

Naif, S., K. Key, S. Constable, and R. L. Evans, 2015, Water-rich bending faults at the Middle America Trench: Geochemistry, Geophysics, Geosystems, **16**, 2582–2597, doi: 10.1002/2015GC005927.

Nelder, J. A., and R. Mead, 1965, A simplex method for function minimization: The Computer Journal, **7**, 308–313, doi: 10.1093/comjnl/7.4.308.

Newman, G. A., and D. L. Alumbaugh, 1997, Three-dimensional massively parallel electromagnetic inversion—I. Theory: Geophysical Journal International, **128**, 345–354, doi: 10.1111/j.1365-246X.1997.tb01559.x.

Newman, G. A., M. Commer, and J. J. Carazzone, 2010, Imaging CSEM data in the presence of electrical anisotropy: Geophysics, **75**, no. 2, F51–F61, doi: 10.1190/1.3295883.

Nozaki, T., T. Nagase, Y. Takaya, T. Yamasaki, T. Otake, K. Yonezu, K. Ikehata, S. Totsuka, K. Kitada, Y. Sanada, Y. Yamada, J. Ishibashi, H. Kumagai, and L. Maeda, and , the D/V Chikyu Expedition 909 Scientists, 2021, Subseafloor sulphide deposit formed by pumice replacement mineralisation: Scientific Reports, **11**, 1–11.

Petersen, S., B. Lehrmann, and B. J. Murton, 2018, Modern seafloor hydrothermal systems: New perspectives on ancient ore-forming processes: Elements, **14**, 307–312, doi: 10.2138/gselements.14.5.307.

Plessix, R.-É., and W. A. Mulder, 2008, Resistivity imaging with controlled-source electromagnetic data: depth and data weighting: Inverse Problems, **24**, 034012, doi: 10.1088/0266-5611/24/3/034012.

Press, W. H., S. A. Teukolsky, B. P. Flannery, and W. T. Vetterling, 1992, Numerical recipes in Fortran 77: Volume 1, Volume 1 of Fortran numerical recipes: The art of scientific computing: Cambridge University Press.

Puzyrev, V., S. Koric, and S. Wilkin, 2016, Evaluation of parallel direct sparse linear solvers in electromagnetic geophysical problems: Computers & Geosciences, **89**, 79–87, doi: 10.1016/j.cageo.2016.01.009.

Safipour, R., S. Hölz, J. Halbach, M. Jegen, S. Petersen, and A. Swidinsky, 2017, A self-potential investigation of submarine massive sulfides: Palinuro Seamount, Tyrrhenian Sea: Geophysics, **82**, no. 6, A51–A56, doi: 10.1190/geo2017-0237.1.

Safipour, R., S. Hölz, M. Jegen, and A. Swidinsky, 2018, A first application of a marine inductive source electromagnetic configuration with remote electric dipole receivers: Palinuro Seamount, Tyrrhenian Sea: Geophysical Prospecting, **66**, 1415–1432, doi: 10.1111/1365-2478.12646.

Sasaki, Y., and M. A. Meju, 2009, Useful characteristics of shallow and deep marine CSEM responses inferred from 3D finite-difference modeling: Geophysics, **74**, no. 5, F67–F76, doi: 10.1190/1.3168616.

Schenk, O., 2022, PARDISO, https://www.pardiso-project.org/, accessed 23 April 2022.

Schenk, O., and K. Gärtner, 2004, Solving unsymmetric sparse systems of linear equations with PARDISO: Future Generation Computer Systems, **20**, 475–487, doi: 10.1016/j.future.2003.07.011.

Schwalenberg, K., M. Haeckel, J. Poort, and M. Jegen, 2010, Evaluation of gas hydrate deposits in an active seep area using marine controlled source electromagnetics: Results from Opouawe Bank, Hikurangi Margin, New Zealand: Marine Geology, **272**, 79–88, doi: 10.1016/j.margeo.2009.07.006.

Schwarzbach, C., R.-U. Börner, and K. Spitzer, 2011, Three-dimensional adaptive higher order finite element simulation for geo-electromagnetics — A marine CSEM example: Geophysical Journal International, **187**, 63–74, doi: 10.1111/j.1365-246X.2011.05127.x.

Sherman, D., P. Kannberg, and S. Constable, 2017, Surface towed electromagnetic system for mapping of subsea Arctic permafrost: Earth and Planetary Science Letters, **460**, 97–104, doi: 10.1016/j.epsl.2016.12.002.

Siripunvaraporn, W., and G. Egbert, 2000, An efficient data-subspace inversion method for 2-D magnetotelluric data: Geophysics, **65**, 791–803, doi: 10.1190/1.1444778.
Siripunvaraporn, W., G. Egbert, Y. Lenbury, and M. Uyeshima, 2005, Three-dimensional magnetotelluric inversion: Data-space method: Physics of the Earth and Planetary Interiors, **150**, 3–14, doi: 10.1016/j.pepi.2004.08.023.
Spagnoli, G., M. Hannington, K. Bairlein, A. Hördt, M. Jegen, S. Petersen, and T. Laurila, 2016, Electrical properties of seafloor massive sulfides: Geo-Marine Letters, **36**, 235–245, doi: 10.1007/s00367-016-0439-5.
Streich, R., 2009, 3D finite-difference frequency-domain modeling of controlled-source electromagnetic data: Direct solution and optimization for high accuracy: Geophysics, **74**, no. 5, F95–F105, doi: 10.1190/1.3196241.
Streich, R., and M. Becken, 2011, Electromagnetic fields generated by finite-length wire sources: Comparison with point dipole solutions: Geophysical Prospecting, **59**, 361–374, doi: 10.1111/j.1365-2478.2010.00926.x.
Von Herzen, R. P., J. Kirklin, and K. Becker, 1996, Geoelectrical measurements at the TAG hydrothermal mound: Geophysical Research Letters, **23**, 3451–3454, doi: 10.1029/96GL02077.
Wang, F., J. P. Morten, and K. Spitzer, 2018, Anisotropic three-dimensional inversion of CSEM data using finite-element techniques on unstructured grids: Geophysical Journal International, **213**, 1056–1072, doi: 10.1093/gji/ggy029.
Weiss, C. J., and S. Constable, 2006, Mapping thin resistors and hydrocarbons with marine EM methods, Part II — Modeling and analysis in 3D: Geophysics, **71**, no. 6, G321–G332, doi: 10.1190/1.2356908.
Weitemeyer, K., and S. Constable, 2014, Navigating marine electromagnetic transmitters using dipole field geometry: Geophysical Prospecting, **62**, 573–596, doi: 10.1111/1365-2478.12092.
Weitemeyer, K. A., S. Constable, and A. M. Tréhu, 2011, A marine electromagnetic survey to detect gas hydrate at Hydrate Ridge, Oregon: Geophysical Journal International, **187**, 45–62, doi: 10.1111/j.1365-246X.2011.05105.x.
Wheelock, B., S. Constable, and K. Key, 2015, The advantages of logarithmically scaled data for electromagnetic inversion: Geophysical Journal International, **201**, 1765–1780, doi: 10.1093/gji/ggv107.
Yamaji, N., N. Okamoto, S. Shiokawa, S. Kawano, and H. Sakurai, 2019, Achievement for pilot test of excavating and ore lifting conducted for seafloor polymetallic sulphides: Journal of MMIJ, **135**, 42–51, doi: 10.2473/journalofmmij.135.42.
Yamane, K., Y. Tuji, K. Akiyoshi, and Y. Nagasaki, 2009, Marine controlled-source electromagnetic sounding for hydrocarbon detection and case study: Journal of the Japanese Association for Petroleum Technology, **74**, 80–91, doi: 10.3720/japt.74.80.
Yuan, J., and R. N. Edwards, 2000, The assessment of marine gas hydrates through electrical remote sounding: Hydrate without a BSR? Geophysical Research Letters, **27**, 2397–2400, doi: 10.1029/2000GL011585.
Zhang, Y., and K. Key, 2016, MARE3DEM: A three-dimensional CSEM inversion based on a parallel adaptive finite element method using unstructured meshes: 86th Annual International Meeting, SEG, Expanded Abstracts, 1009–1013, doi: 10.1190/segam2016-13681445.1.
Zhdanov, M. S., M. Endo, L. H. Cox, M. Čuma, J. Linfoot, C. Anderson, N. Black, and A. V. Gribenko, 2014, Three-dimensional inversion of towed streamer electromagnetic data: Geophysical Prospecting, **62**, 552–572, doi: 10.1111/1365-2478.12097.
Zhu, Z., C. Tao, J. Shen, A. Revil, X. Deng, S. Liao, J. Zhou, W. Wang, Z. Nie, and J. Yu, 2020, Self-potential tomography of a deep-sea polymetallic sulfide deposit on southwest Indian ridge: Journal of Geophysical Research, Solid Earth, **125**, e2020JB019738, doi: 10.1029/2020JB019738.

Biographies and photographs of the authors are not available.